nature neuroscience

ARTICLES

https://doi.org/10.1038/s41593-020-00759-4

Long-term self-renewing stem cells in the adult mouse hippocampus identified by intravital imaging

Sara Bottes[1,9], Baptiste N. Jaeger[1,9], Gregor-Alexander Pilz[1,9], David J. Jörg[2,3,4], John Darby Cole[1], Merit Kruse[1], Lachlan Harris[5], Vladislav I. Korobeynyk[1], Izaskun Mallona[6,7], Fritjof Helmchen[8], François Guillemot[5], Benjamin D. Simons[2,3,4] and Sebastian Jessberger[1]✉

Neural stem cells (NSCs) generate neurons throughout life in the mammalian hippocampus. However, the potential for long-term self-renewal of individual NSCs within the adult brain remains unclear. We used two-photon microscopy and followed NSCs that were genetically labeled through conditional recombination driven by the regulatory elements of the stem cell-expressed genes GLI family zinc finger 1 (*Gli1*) or achaete-scute homolog 1 (*Ascl1*). Through intravital imaging of NSCs and their progeny, we identify a population of Gli1-targeted NSCs showing long-term self-renewal in the adult hippocampus. In contrast, once activated, Ascl1-targeted NSCs undergo limited proliferative activity before they become exhausted. Using single-cell RNA sequencing, we show that Gli1- and Ascl1-targeted cells have highly similar yet distinct transcriptional profiles, supporting the existence of heterogeneous NSC populations with diverse behavioral properties. Thus, we here identify long-term self-renewing NSCs that contribute to the generation of new neurons in the adult hippocampus.

In contrast to many organs, the adult mammalian brain shows poor regenerative capacity and fails to replace neurons that become dysfunctional or those lost through acute or chronic injury. However, the discovery of NSCs within discrete regions of the adult brain opened up the possibility to harness these cells for endogenous brain repair[1]. Despite some conflicting results regarding the human brain, the hippocampal dentate gyrus (DG) seems to be among the brain areas that generate new neurons throughout life[2–8]. Within the DG, NSCs generate new excitatory granule cells that are important for a variety of hippocampal functions[3]. Previous work identified the cellular and molecular identity of neurogenic cells in the DG with largely quiescent radial glia-like cells (R or type I cells) that give rise to more rapidly cycling nonradial glia-like cells (NR or type II cells)[9–11]. However, it remained controversial, due to ambiguity when recovering lineage information from static pulse-chase lineage-tracing assays, whether NSCs that exist in the DG possess long-term self-renewal potential (that is, renewing through cell division while giving rise to differentiated progeny) or whether activation of NSCs leads to their rapid depletion from the stem cell pool via terminal differentiation[12–16]. Exhaustion of NSCs upon initial activation may explain the dramatic decrease in hippocampal neurogenesis by around 80% from 2 to 8 months of age in the rodent brain[3,17–19]. However, neurogenesis plateaus and continues throughout the entire life span, albeit at low levels, which may be due to increased quiescence of aged NSCs compared to NSCs in the young hippocampus[20]. Theoretical modeling approaches suggest that long-term self-renewal may be required to sustain neurogenesis throughout life, but experimental evidence remains scant[12,21]. To probe directly the potential for long-term self-renewal of individual NSCs in the adult DG, we used intravital imaging together with single-cell RNA sequencing (scRNA-seq) to analyze the molecular and behavioral properties of Gli1-targeted NSCs and compared them to Ascl1-targeted neurogenic cells[16].

Results

Gli1 lineages contain long-term self-renewing clones. Using static analyses of individual time points, we found that low-dose tamoxifen (Tam)-induced recombination in *Gli1-Cre*^{ERT2} mice crossed with a tdTomato reporter mouse line sparsely labeled neurogenic cells in the subgranular zone of the DG (Fig. 1a)[22]. The number and spatial distribution of recombined cells was comparable between *Gli1*- and *Ascl1-Cre*^{ERT2} lines (Extended Data Fig. 1a–f and Supplementary Movie 1). Soon after Tam administration, recombined cells showed the morphology of radial glia-like NSCs (hereafter called R cells)[10,11]. In contrast to Ascl1-targeted cells, only a small fraction (~5%) of Gli1-targeted cells in the DG showed morphological features and marker expression of nonradial precursors (hereafter NR cells) soon after Tam administration (Fig. 1a and Extended Data Fig. 1g). By using single-molecule RNAscope technology, we corroborated previous results[23] showing that the pro-activation factor Ascl1 exhibits comparable mRNA levels in activated (ki67$^+$) and quiescent (ki67$^-$) Gli1- and Ascl1-targeted R cells. Additionally, we found slightly higher Ascl1 expression levels in Gli1- compared to Ascl1-targeted dividing NR cells and in ki67$^+$ Gli1- compared to

[1]Laboratory of Neural Plasticity, Faculties of Medicine and Science, Brain Research Institute, University of Zurich, Zurich, Switzerland. [2]Wellcome Trust-Medical Research Council Stem Cell Institute, University of Cambridge, Cambridge, UK. [3]The Wellcome Trust/Cancer Research UK Gurdon Institute, University of Cambridge, Cambridge, UK. [4]Department of Applied Mathematics and Theoretical Physics, Centre for Mathematical Sciences, University of Cambridge, Cambridge, UK. [5]Neural Stem Cell Biology Laboratory, The Francis Crick Institute, London, UK. [6]Institute of Molecular Life Sciences and SIB Swiss Institute of Bioinformatics, University of Zurich, Zurich, Switzerland. [7]Department of Molecular Mechanisms of Disease, University of Zurich, Zurich, Switzerland. [8]Laboratory of Neural Circuit Dynamics, Faculties of Medicine and Science, Brain Research Institute, University of Zurich, Zurich, Switzerland. [9]These authors contributed equally: Sara Bottes, Baptiste N. Jaeger, Gregor-Alexander Pilz. ✉e-mail: jessberger@hifo.uzh.ch

ki67+ Ascl1-targeted cells (Extended Data Fig. 1h–k). Using immunohistochemistry, we found that Gli1-targeted R and NR cells expressed a previously described set of marker proteins (Fig. 1a).

To follow individual Gli1-targeted R cells over time, we used chronic intravital imaging of sparsely labeled hippocampal NSCs (Fig. 1b,c)[16]. Gli1-targeted R cells became recruited into the proliferating pool of neurogenic cells over time (Fig. 1d–g, Supplementary Fig. 1 and Supplementary Movies 2 and 3). The fraction of R cells remaining quiescent over the time course was higher in Gli1-targeted R cells compared to Ascl1-targeted R cells, while entry into the cell cycle occurred throughout the imaging period (Fig. 1h,i and Extended Data Fig. 2a). Hippocampal window implantation and imaging did not substantially affect proliferation, R cell activation or cellular output of sparsely labeled Gli1-targeted cells (Extended Data Fig. 2b–h). Moreover, it did not cause significant gliosis and inflammation in the ipsilateral side of the DG compared to the contralateral side (Extended Data Fig. 2i–k). Once Gli1-targeted R cells entered the cell cycle, they produced an average of five granule neurons (Fig. 1j and Extended Data Fig. 2a). Most strikingly, we found that some Gli1-targeted R cells returned to quiescence after producing progeny (Fig. 1d,e and Supplementary Fig. 1).

The fraction of long-term self-renewing R cells was substantially higher in Gli1-targeted clones compared to Ascl1-targeted clones, with no unambiguously identifiable Ascl1-targeted R cells surviving over a 30-d period following activation (Fig. 2a–c and Extended Data Fig. 2a). By contrast, a fraction of Gli1-targeted R cells produced progeny and persisted for more than 56 d upon activation, with one clone showing at least 100 d of self-renewal (Fig. 2a), indicating that the adult DG harbors NSCs with long-term self-renewal capacity. Thus, Gli1-mediated recombination labels an adult NSC population that retains the ability to self-renew over extended periods, whereas Ascl1-targeted clones label R cells that become exhausted upon activation (Fig. 2a,b,d). Although the average activation time of Gli1-targeted R cells was also significantly longer than that of Ascl1-targeted R cells (Fig. 1i), there was no correlation between the time to first division and self-renewal duration of R cells (Extended Data Fig. 3a).

As further evidence of distinct behavioral features of NSC populations in the adult DG, we found that Gli1-targeted R cells showed a higher abundance of symmetric (duplicative) divisions and more asymmetric (renewing) divisions over consecutive cell divisions as compared to Ascl1-targeted cells (Fig. 2f–i)[16]. This was also reflected in distinct cell division characteristics: Gli1-targeted R cells had significantly longer time intervals between consecutive R cell divisions but showed higher total numbers of cell divisions (Fig. 2e,f and Supplementary Fig. 1). The comparison of the time between divisions among different successive R divisions (counted from the first asymmetric R division) in each mouse line revealed no differences in either Gli1- or Ascl1-targeted R cells, suggesting that this timescale does not change according to the division history of the cell (Extended Data Fig. 3b). However, the average time between divisions was significantly higher in Gli1- compared to Ascl1-targeted R cells, in accordance with the average time between R cell divisions for each clone shown in Fig. 2e (Extended Data Fig. 3b). Moreover, by clustering cell lineages using a set of predefined core characteristics (Methods), we found a preferential clustering of Gli1- versus Ascl1-targeted clones, supporting the partial behavioral diversity of these two genetically targeted lineages (Fig. 2j).

In contrast to R cells, we found that the behavior of NR cells was remarkably similar between Gli1- and Ascl1-derived lineages regarding cell division kinetics and lineage choices (Fig. 2i and Extended Data Fig. 3c–e). Thus, long-term intravital imaging-derived data indicate functional heterogeneity of R cells within the adult hippocampus, identifying a long-term self-renewing NSC population targeted by the Gli1 promoter and a second population, targeted by the Ascl1 promoter, with only short-term renewal potential.

Molecular diversity of Gli1- and Ascl1-targeted lineages. The observed differential behavior of Gli1- versus Ascl1-targeted cell lineages may be explained by (1) diverse sets of NSC populations, (2) a hierarchical organization in which Gli1-targeted NSCs with long-term renewal potential give rise to Ascl1-targeted NSCs with limited renewal potential or (3) the alignment of NSCs along a spectrum of diminishing renewal potential. To seek independent evidence for potential sub-lineage relationships, we used fluorescence-activated cell sorting (FACS) to isolate Gli1- and Ascl1-targeted cells directly from the adult hippocampus at different time points after Tam-induced recombination followed by deep scRNA-seq using Smart-Seq2 (Fig. 3a and Extended Data Fig. 4a). As expected, we found distinct populations of cells using uniform manifold approximation and projection (UMAP) and *t*-distributed stochastic neighbor embedding (*t*-SNE) that segregated robustly into clusters of nondividing NSCs (ndNSCs), dividing NSCs (dNSCs), immature neurons (INs) and mature neurons (MNs) for both Gli1- and Ascl1-targeted populations (Fig. 3b,c and Extended Data Fig. 4b). All four clusters could be identified 5 d and 12 weeks after Tam-induced recombination (Fig. 3d and Extended Data Fig. 4c), albeit the relative numbers of cell-specific profiles shifted with time, consistent with the in vivo live-imaging data (Fig. 3d and Extended Data Fig. 4d,e). In line with the RNAscope data (Extended Data Fig. 1h–k), *Ascl1* mRNA was expressed at the same level in Gli1- and Ascl1-targeted ndNSCs but showed moderately higher expression levels in Gli1- compared to Ascl1-targeted dNSCs (Extended Data Fig. 4f,g). Since the dNSC cluster likely

Fig. 1 | Gli1-targeted R cells contain long-term self-renewing hippocampal stem cells. a, Representative confocal images of R (tdTom+, SOX2+ and Nestin+; red arrow; white arrowhead indicates major radial R cell process) and NR (tdTom+, SOX2+ and Nestin−; orange arrow) cells after recombination with imaging dose. Quantification of tdTom+ cell types in the subgranular zone 2 d after recombination. **b**, Experimental setup for chronic in vivo imaging of Gli1-tdTom NSCs over up to 100 d. Image shows a representative R cell. **c**, Representative in vivo images of a Gli1-targeted quiescent R cell at 4 and 102 d post inoculation (d.p.i.) and post hoc immunohistochemical analysis of the same R cell (tdTom+, SOX2+ and GFAP+; white arrowhead indicates major radial process) at 102 d.p.i. The horizontal view of the cell corresponds to the view obtained during in vivo imaging. **d**, Selected images (collapsed *z*-stacks) of a Gli1-targeted R cell (white arrowhead) and its progeny imaged over the course of 2 months exhibiting long-term self-renewal (51 d). Post hoc immunohistochemical analysis of the same clone (tdTom+) at 61 d.p.i. **e**, Lineage tree deduced from tracking the R cell in **d**. Identified cell types are color coded, and lineage transitions are depicted depending on their certainty (Methods). **f**, Example of a Gli1-targeted R cell clone showing long R cell persistence. Post hoc immunohistochemical analysis of the same clone (tdTom+, SOX2+ and GFAP+) at 102 d.p.i. shows the presence of an R cell (white arrowhead, GFAP+SOX2+), an NR cell (GFAP−SOX2+) and a neuron (GFAP−SOX2−). **g**, Lineage tree deduced from tracking the R cell in **f** and its progeny. N, neuron. **h**, Percentage of active and quiescent clones in Gli1- and Ascl1-targeted cells (total Gli1 (*n*): 136; Gli1 active: 41.1%; Gli1 quiescent: 58.8%; total Ascl1 (*n*): 80; Ascl1 active: 71.2%; Ascl1 quiescent: 28.75%). Ascl1 cell data consist of 19 new lineages and 61 previously described lineages (Methods). **i**, Time (d) until the first division of Gli1 and Ascl1 R cells calculated from the start of the imaging 2 d.p.i. (Gli1: 24.98 ± 2.8 d, $n = 56$ R cells; Ascl1: 11.85 ± 1.5 d, $n = 57$ R cells; Mann–Whitney test: Mann–Whitney $U = 1{,}055$; $^{**}P = 0.0017$, two-tailed). **j**, Final number of cells per active clone (Gli1: 5.03 ± 0.57, $n = 56$ clones; Ascl1: 5.86 ± 0.64, $n = 57$ clones; Mann–Whitney $U = 1{,}440$; $P = 0.3699$, two-tailed). NS, not significant. Circles represent individual clones. Values are the mean ± s.e.m. Scale bars, 10 µm (**a**, **c** and staining in **f**), 20 µm (staining in **d**), 25 µm (**f**) and 50 µm (**d**). For detailed statistics, see Supplementary Table 5.

encompassed R and NR cells, we sought to investigate the heterogeneity of this cluster. Despite regressing out cell cycle genes, we were unable to further divide the dNSCs into subclusters based on the expression patterns of key marker genes for radial NSCs (for example, *Hopx*, *Nestin*, *Gfap*, *Spot14*/*Thrsp* and *Sox2*) versus nonradial NSCs (*Tbr2*/*Eomes* and *Sox2*; data not shown).

We next performed lineage inference analysis using Slingshot[24], which confirmed a developmental trajectory from ndNSCs via dNSCs to mature neurons (Fig. 3e). In accordance with the imaging-based data, we found that the relative number of sequenced ndNSCs was substantially higher in Gli1-targeted cells compared to Ascl1-targeted cells (Fig. 3f). We then asked whether

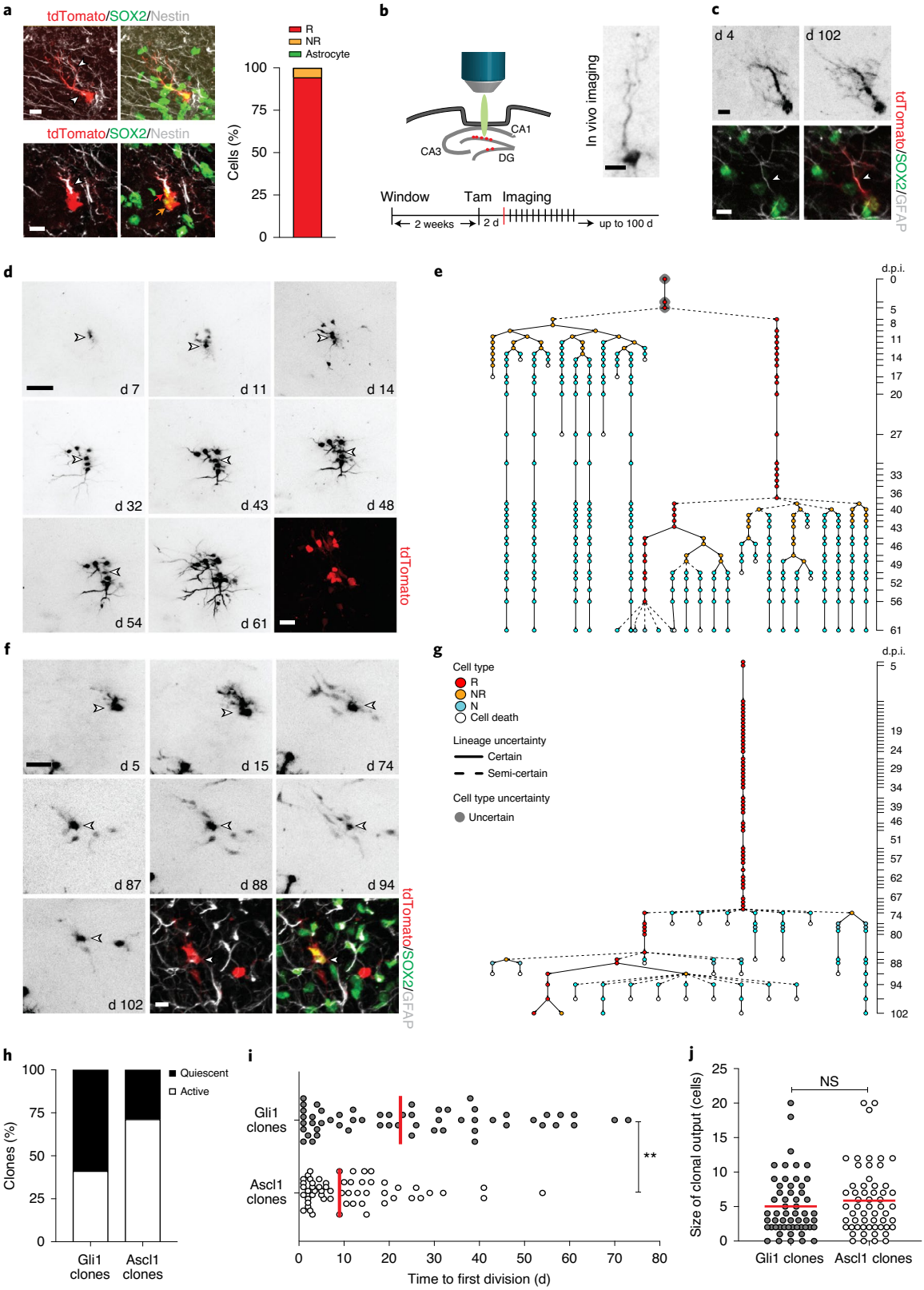

NSC populations may differ in their developmental maturity using pseudotime-based alignment; indeed, we found that Gli1-targeted ndNSCs appeared to be further distant from neuronal progeny compared to Ascl1-targeted nondividing R cells, suggesting that at least a fraction of Gli1-targeted R cells may be in a more quiescent/undifferentiated state compared to Ascl1-targeted R cells (Fig. 3g). Despite the high level of similarity in the gene expression pattern between Gli1- and Ascl1-targeted cells, some genes were differentially expressed between ndNSCs and dNSCs derived from Gli1- or Ascl1-targeted cells (Fig. 3h–j and Supplementary Tables 1 and 2). To verify that these differentially expressed genes (DEGs) did not only result from the small proportion of outlier cells occupying earlier (Gli1) or later (Ascl1) areas of the pseudotime, we performed a differential expression analysis only between Gli1 and Ascl1 cells that shared the same pseudotime range (Extended Data Fig. 4h). Comparison between DEGs identified in the presence or absence of the pseudotime outliers only revealed a minor influence of the outliers on the top DEGs (Extended Data Fig. 4i,j). While Gli1 and Ascl1 lines do not label entirely distinct NSC populations, our results suggest that the DEGs identified between Gli1- and Ascl1-targeted NSCs are not only driven by a small proportion of pseudotime outliers but rather reflect inherent transcriptional differences between these two lines. Notably, we identified several genes that had been previously implicated in NSC quiescence and self-renewal to be differentially expressed between Gli1- and Ascl1-targeted NSCs, among others including metallothionein-3 (*Mt3*), diazepam-binding inhibitor (*Dbi*) and *Hopx*[25–27]. These findings suggest that the identified gene set expressed at high levels in Gli1-targeted NSCs may be highly relevant in governing NSC self-renewal.

Based on the intravital imaging data, we expected to detect transcriptional profiles that may indicate the return to quiescence after activation in Gli1-targeted cells. To probe for this, we analyzed the relative abundance of nascent and mature mRNA in each cell as an indicator of the future state of the cell using RNA velocity in Gli1- and Ascl1-targeted cells[28]. While most dNSCs showed a positive velocity directed toward immature neurons, a fraction of dNSCs showed a negative velocity pointing toward ndNSCs. We confirmed this velocity pattern with a different RNA velocity method that takes into account the full transcriptional dynamics of splicing kinetics using a likelihood-based dynamical model scVelo[29] (Extended Data Fig. 4k). Using an independent dataset[30], Bergen and colleagues also found that radial-glial cells harbor a velocity vector pointing away from the neuronal differentiation path[29], further supporting our observations. Interestingly, activated Gli1-targeted NSCs showed a higher fraction of cells with such negative velocities as compared to Ascl1-targeted cells (Fig. 4a,b). We next compared DEGs between dNSCs with negative versus positive velocities and found that those with negative velocities upregulated a set of genes previously implicated in NSC quiescence, such as *Thrsp* (*Spot14*) and *ApoE*, and downregulated genes associated with cell division such as the cell division cycle-associated protein 4 (*Cdca4*; Fig. 4c and Supplementary Table 3)[9,31,32]. These findings confirm the presence of NSCs, enriched in the Gli1-targeted population that shows transcriptional dynamics indicative of a return to a quiescent state.

Hopx and Mt3 protein levels differentiate between Gli1- and Ascl1-targeted R cells. We next asked whether the identified DEGs also showed distinct expression profiles at the protein level. We established a modified iterative indirect immunofluorescence imaging (4i) technology for use on tissue sections, allowing for the consecutive antibody-based analyses of up to 20 different proteins[33]. We first confirmed that both Gli1- and Ascl1-targeted cells expressed commonly used markers of R cells such as SOX2, GFAP and Id4 (Extended Data Fig. 5a,b). We next analyzed the expression of Hopx, recently associated with stem cell activity and self-renewal capacity of postnatal NSCs[9,26,34]. In accordance with the mRNA expression profiles, we found that Hopx protein was expressed in virtually all R cells analyzed that were targeted by the Gli1 or Ascl1 promoter (Fig. 4d and Extended Data Fig. 5b,d). However, Hopx protein levels were significantly higher in Gli1-targeted cells compared to Ascl1-targeted cells, indicating that differences in *Hopx* mRNA expression were also translated into distinct protein expression differences between Gli1- and Ascl1-targeted R cells. Protein expression levels of other stem cell-associated proteins such as SOX2 were comparable between Gli1- and Ascl1-targeted NSCs (Extended Data Fig. 5e). To further substantiate these findings, we found that metallothionein-3 (*Mt3*), showing differentially expressed mRNA levels (Fig. 3h,i), was also differentially expressed at the protein level (Fig. 4d and Extended Data Fig. 5b). Moreover, negative cells for Mt3 protein expression also showed lower levels of Hopx protein (Extended Data Fig. 5f).

Single-cell gene expression predicts molecular origin of hippocampal R cells. Based on the differential expression of a subset of core genes in Gli1- and Ascl1-targeted cells in both ndNSCs and dNSCs (Fig. 3h,i), we next asked whether commonly used machine-learning strategies, such as random forest classifier (RFC), k-nearest neighbor (k-NN) and generalized linear models (GLM), may allow for prediction of cellular origin (Fig. 4e).

Fig. 2 | Diverse behavioral features of Gli1- and Ascl1-targeted NSCs. a, Self-renewal duration (time (d) between first and last division in each lineage) of Gli1- and Ascl1-targeted R cells (Gli1: 17.80 ± 2.5 d, $n = 56$ clones; Ascl1: 6.5 ± 0.9 d, $n = 57$ clones; Mann–Whitney $U = 931$; $^{****}P < 0.0001$, two-tailed). Triangles depict clones where R cells were still present at the end of the imaging (reported only for the clones with observed self-renewal duration of ≥28 d). The described self-renewal duration of these clones is an underestimation of their actual capacity. Red circles depict R cells showing long-term self-renewal. The dashed line represents a long-term self-renewal threshold (30 d). **b**, Fraction of clones with different R content (0R, 1R, 2R and 3R cells) over time, normalized to the surviving population. All (certain, semi-certain and uncertain) R cells were considered. Lineage trees shifted to the first R cell division time point. **c**, Percentage of clones with R cell self-renewal of ≥30 d (Gli1: 19.64%, $n = 56$ clones; Ascl1: 0%, $n = 57$ clones). Only R cells that were classified as certain are considered. **d**, Average clone content for Gli1 and Ascl1 lineages over time. **e**, Average time (d) between R cell divisions (Gli1: 10.71 ± 2.4 d, $n = 37$ clones; Ascl1: 3.64 ± 0.5 d, $n = 41$ clones; Mann–Whitney $U = 337.5$; $^{****}P < 0.0001$, two-tailed). **f**, Number of successive R cell division rounds 1 to 4 in Gli1 and Ascl1 lineages (Gli1: 33.93% (1), 35.71% (2), 19.64% (3) and 10.71% (4), $n = 56$ clones; Ascl1: 28.07% (1), 50.88% (2), 19.30% (3) and 1.75% (4), $n = 57$ clones). **g**, Percentage of asymmetric proliferative R divisions (R mother cell generates one R daughter cell and one NR daughter cell) in division rounds 1 to 4 (Gli1: 77.78% (1), $n = 27$ divisions; Gli1: 47.37% (2), $n = 19$ divisions; Gli1: 54.55% (3), $n = 11$ divisions; Gli1: 25.0% (4), $n = 4$ divisions. Ascl1: 77.5% (1), $n = 40$ divisions; Ascl1: 31.03% (2), $n = 29$ divisions; Ascl1: 12.5% (3), $n = 8$ divisions). **h**, Percentage of symmetric duplicating R cell divisions in the first division (Gli1: 18.52%, $n = 27$ divisions; Ascl1: 7.50%, $n = 40$ divisions). **i**, Heat map representing the frequencies of modes of division of Gli1- targeted R cells (division round (Div) 1: $n = 27$ divisions; 2: $n = 19$ divisions; 3: $n = 11$ divisions; 4: $n = 4$ divisions) and Ascl1-targeted R cells (Div 1: $n = 40$ divisions; 2: $n = 29$ divisions; 3: $n = 8$ divisions). A, astrocyte. **j**, Lineage tree clustering using the Ward's hierarchical clustering method. Gli1 lineages are contained in cluster 1 (45.4%) and cluster 2 (54.6%). Ascl1 lineages are in cluster 1 (7.0%) and cluster 2 (93.0%). Cluster 1 consists of 86.2% Gli1 lineages and 13.8% Ascl1 lineages. Cluster 2 consists of 36.1% Gli1-derived lineages and 63.9% Ascl1-derived lineages. Circles in **a** and **e** represent individual clones. Values are the mean ± s.e.m. For detailed statistics, see Supplementary Table 5.

Strikingly, all three models were able to predict accurately Gli1- versus Ascl1-derived nondividing and dividing R cells (Fig. 4g). These findings suggest that, despite the high transcriptional similarity overall and the partial overlap in behavior, significant differences exist in the targeted populations that allow for predictions of the cellular origin of profiled cells. Thus, manipulating their expression levels in adult NSCs may represent a future entry point to alter the functional behavior of neurogenic cells in the adult brain.

Discussion

We used chronic intravital imaging and mRNA and protein analyses to define the functional and molecular properties of individual NSCs and their progeny targeted through Gli1- and Ascl1-promoters within the adult hippocampus. We find that a fraction of Gli1-targeted NSCs show evidence of long-term self-renewal, producing progeny for months following initial activation. In contrast, once activated, Ascl1-targeted R cells produce a burst of neurogenic activity before

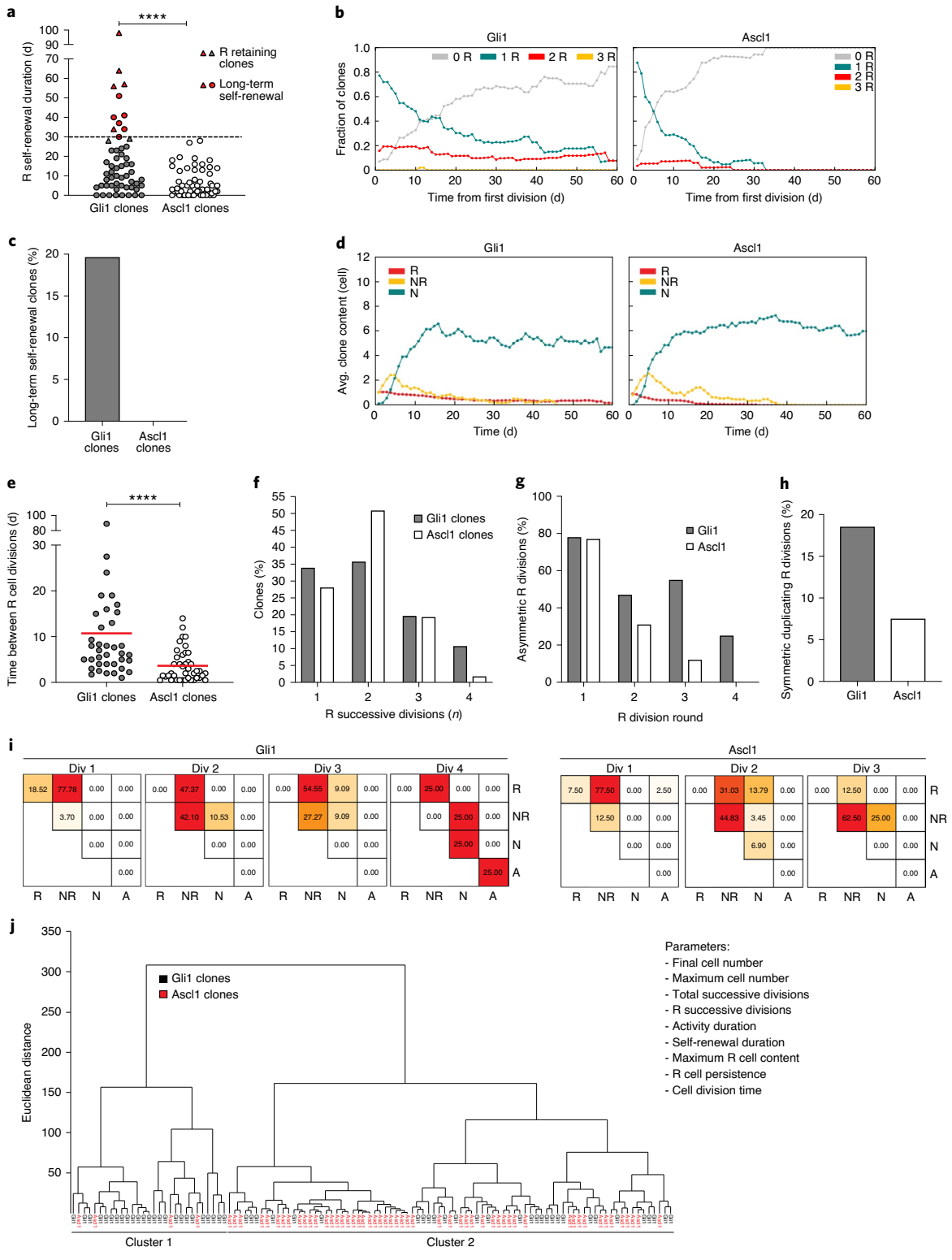

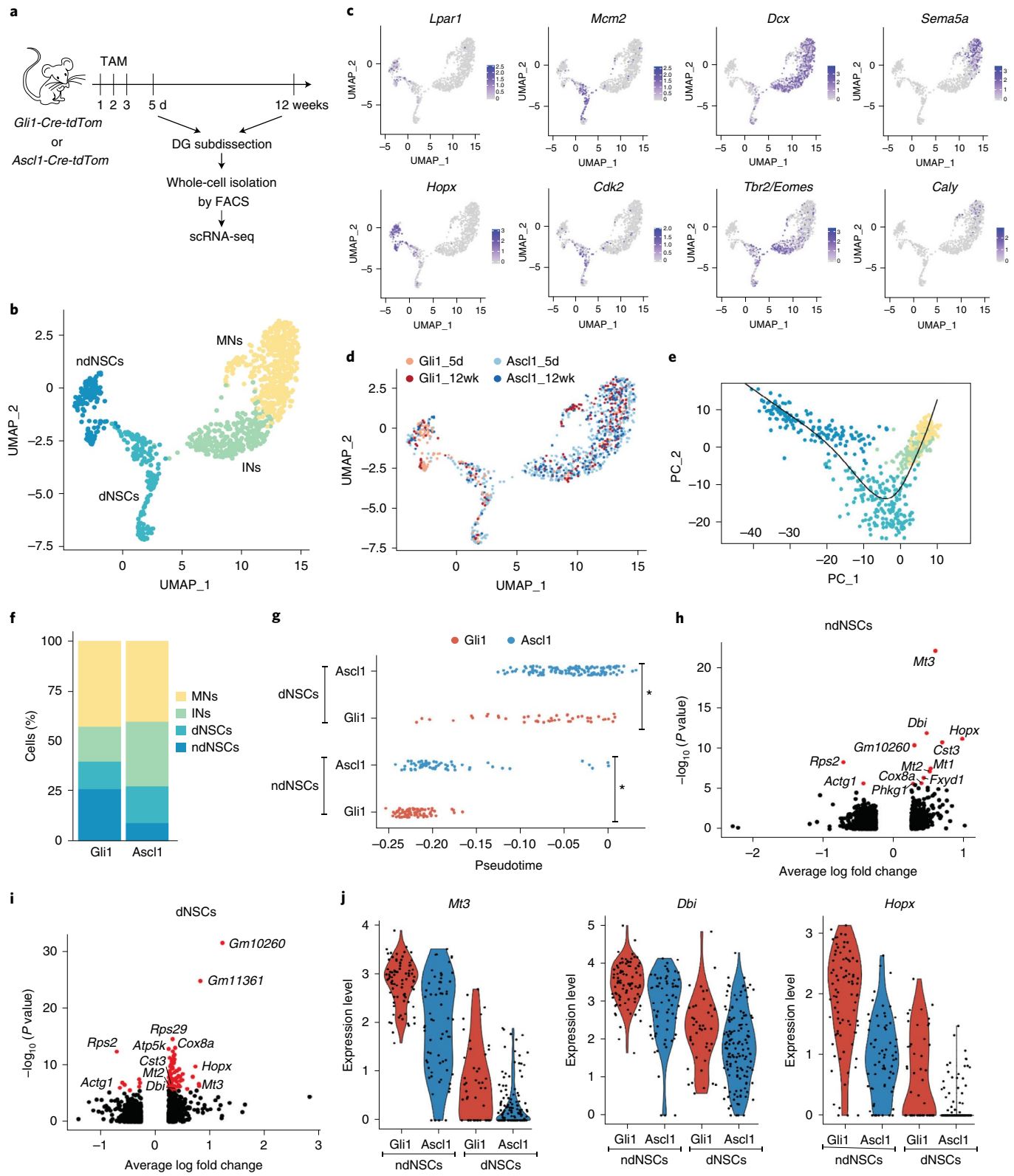

Fig. 3 | scRNA-seq of Gli1- and Ascl1-targeted cells identifies NSCs with self-renewal potential. a, Overview of the experimental approach. **b**, UMAP visualization of the four clusters identified in Gli1- and Ascl1-targeted tdTomato$^+$ neuronal cells. **c**, Expression patterns of two cluster-specific genes for ndNSCs (far left), dNSCs (left), INs (right) and MNs (far right). **d**, Gli1- and Ascl1-targeted tdTomato$^+$ cells isolated 5 d (Gli1_5d and Ascl1_5d, respectively) or 12 weeks (Gli1_12wk and Ascl1_12wk, respectively) after the last Tam injection displayed on the UMAP plot from **b**. **e**, Lineage inference analysis. **f**, Percentages of ndNSCs, dNSCs, INs and MNs among all Gli1- or Ascl1-targeted cells. **g**, Position of Gli1 and Ascl1 ndNSCs and dNSCs along the pseudotime axis as calculated by Monocle. Unpaired *t*-test; ndNSCs: $P = 2.55 \times 10^{-6}$; dNSCs: $P = 0.0004042$; $^*P < 0.05$. **h**,**i**, Volcano plots showing significant DEGs (red; adjusted P (P_{adj}) < 0.05) between Gli1- or Ascl1-targeted ndNSCs (**h**) or dNSCs (**i**). Bolded gene names highlight DEGs found in both ndNSC (**h**) and dNSC (**i**) comparisons. **j**, Violin plots showing the top three common DEGs. For detailed statistics, see Supplementary Table 5.

they terminally differentiate within weeks (Fig. 4g). Thus, the data presented here reconcile previously conflicting results regarding the self-renewal capacity of hippocampal NSCs, identifying functional diversity of neurogenic NSCs within the adult DG[15,35]. We show that behavioral states of NSCs in the adult hippocampus are heterogeneous and consist of R cells that become exhausted upon activation and R cells that retain the ability to self-renew over the longer term. These imaging-based findings, which are consistent with previous interpretations of snapshot-based static data[12], may be explained by three alternative scenarios: (1) two types of NSCs exist in the adult DG, one showing long-term self-renewal and the other rapid exhaustion upon activation, (2) Gli1-targeted cells may be developmentally upstream of Ascl1-targeted cells or (3) the behavior of NSCs distributes along a spectrum of self-renewal potential with

Fig. 4 | Molecular profiling reveals distinct features of Gli1- versus Ascl1-targeted NSCs. a, The observed and the extrapolated future states (arrows) of Gli1 or Ascl1 cells were calculated using RNA velocity. The velocities are visualized on the UMAP plot from Fig. 3b. Velocity estimates were based on nearest-cell pooling ($k = 300$). **b**, Percentages of Gli1 or Ascl1 dNSCs with a velocity vector directed toward ndNSCs (yellow quadrants: vector angles between 180° and 360°). **c**, Volcano plot showing significant DEGs (red; $P_{adj} < 0.05$) between dNSCs displaying an RNA velocity vector directed toward ndNSCs (yellow quadrants: vectors between 180° and 360°) or INs (green quadrants: vectors between >0° and <180°). Bolded gene names highlight common DEGs in volcano plots (Fig. 3h,i). **d**, Top: representative examples of Gli1 and Ascl1 R cells (arrowheads) stained using the 4i protocol, 5 d after Tam injection. Visualization of single channels: tdTom, Hopx and Mt3. Bottom: quantification of Hopx (Gli1: 7.62 ± 0.197, $n = 337$ cells; Ascl1: 6.14 ± 0.177, $n = 316$ cells; unpaired t-test: $t = 5.532$; df = 651; ***$P < 0.0001$, two-tailed) and Mt3 (Gli1: 2.72 ± 0.064, $n = 337$ cells; Ascl1: 2.34 ± 0.065, $n = 318$ cells; unpaired t-test: $t = 4.201$; df = 653; ***$P < 0.0001$, two-tailed) protein levels (fluorescence intensity of the cell over background intensity) in Gli1- and Ascl1-targeted R cells. **e**, Schematic of the machine-learning approach. Both ndNSCs and dNSCs from Gli1- and Ascl1- targeted cells were divided into a training and a testing set (1:1). The nine DEGs found in both ndNSC (Fig. 3h) and dNSC (Fig. 3i) comparisons were used to build three different machine-learning models for classification: RFC, k-NN and GLM. The genotype (Gli1 or Ascl1) of ndNSCs and dNSCs was than predicted using the three classification models. **f**, Numbers and prediction accuracy rates to classify Gli1- versus Ascl1-targeted cells using RFC, k-NN and GLM models together. Shades of red represent the accuracy of the prediction. **g**, Schematic showing the differential behavior of the two NSC populations in the DG: the first one gives rise to a burst of neurogenic activity followed by depletion of the NSC; the second can perform long-term self-renewal contributing to stem cell niche maintenance. Values are reported as the mean ± s.e.m. Bars in violin plots represent the median and upper and lower quartiles. Scale bars, 20 µm (**d**). For detailed statistics, see Supplementary Table 5.

Gli1 targeting NSCs mostly at one end and Ascl1 targeting NSCs largely at the opposing end of the spectrum.

Some observations support a bona fide diversity of NSCs in the adult DG. First, cell division kinetics and patterns of intermediate quiescence between subsequent divisions (Fig. 2e–i and Extended Data Fig. 3b) are distinct between Ascl1- and Gli1-targeted cells, indicating that Ascl1 lineages cannot be superimposed onto Gli1-targeted lineages straightforwardly. Second, deep sequencing of single Gli1- and Ascl1-targeted R cells showed subtle but decisive differences in gene expression. Although a certain overlap exists at the single-cell level, these differential gene expression results are not driven by a small proportion of outlier cells in each group and are also reflected at the protein level (that is, Hopx and Mt3), allowing for the separation of Gli1- versus Ascl1-targeted cells (Figs. 3h–j and 4d–f). However, other findings are consistent with the hypothesis that Gli1-targeted R cells are upstream of Ascl1-targeted cells: we found that Gli1-targeted R cells appeared to be more undifferentiated based on pseudotiming analyses (Fig. 3g); furthermore, the behavior of NR cells was remarkably similar between Gli1- and Ascl1-targeted cells (Extended Data Fig. 3c–e).

Finally, further aspects of our data suggest that the behavior of NSCs aligns along a spectrum of stem cell potential. Firstly, not only Gli1-targeted R cells but also a small fraction of Ascl1-targeted R cells (~8%) show symmetrical cell division following initial activation (that is, generating two daughter R cells through duplication). However, in the 56 active lineages analyzed, we never observed symmetric (duplicative) divisions in the second or later rounds of division of Gli1-targeted R cells, as would be expected if Gli1-targeted R cells give rise to Ascl1-targeted R cells. Secondly, although individual NSCs can exhibit distinct and diverse behaviors once activated, Ascl1- and Gli1-mediated targeting do not label two completely distinct NSC populations as suggested by the partial overlap in molecular profiles and behaviors. For example, the hierarchical clustering (Fig. 2j) shows a mixture of Gli1 and Ascl1 clones in both clusters, albeit in different proportions. Therefore, it is plausible that each line biases toward one behavior and away from another along a spectrum of renewal potential, and that factors such as local microenvironmental cues may determine where a given NSC falls along this spectrum.

To discriminate among these scenarios, future experiments will need to combine intravital imaging with intersectional genetic lineage-tracing approaches and/or targeted ablation of Gli1- versus Ascl1-targeted NSCs. However, the application of these approaches in combination is extremely challenging and currently not feasible. Despite distinct behavioral properties of Gli1-targeted R cells compared to Ascl1-targeted R cells, mRNA expression profiles were remarkably similar, albeit not identical between Gli1- and Ascl1-targeted populations, and we confirmed the differential expression levels of candidate genes at the protein level (that is, Mt3 and Hopx). Clearly, cell fate may be directed through mechanisms independent of gene transcription/expression, by modifying signaling activity through transcription-independent mechanisms[12–14]. In addition, Ascl1- and Gli1-targeted populations are not discrete but they do overlap. Thus, future studies using more extensive single-cell deep sequencing and/or unbiased expression analyses of not only transcripts but also translated proteins on a single-cell level will be needed to identify the detailed molecular differences mediating behavioral diversity of adult hippocampal NSCs. Future experiments could also modify the imaging protocol to fully rule out the possibility that chronic exposure to gas anesthesia, surgery or window implantation may have some effect on neurogenesis. However, the identification of long-term self-renewal in Gli1-targeted and not in Ascl1-targeted NSCs supports the validity of our observations and approach. Using chronic in vivo imaging and single-cell molecular analyses, our data resolve functional heterogeneity of NSCs within the adult brain. Thus, the data presented here identify long-term self-renewing NSCs in the hippocampus and characterize the molecular and cellular framework to direct distinct behaviors of R cells with the aim to enhance neurogenesis for regenerative repair in the adult brain.

Online content

Any methods, additional references, Nature Research reporting summaries, source data, extended data, supplementary information, acknowledgements, peer review information; details of author contributions and competing interests; and statements of data and code availability are available at https://doi.org/10.1038/s41593-020-00759-4.

Received: 19 November 2019; Accepted: 13 November 2020;
Published online: 21 December 2020

References

1. Gage, F. H. Adult neurogenesis in mammals. *Science* **364**, 827–828 (2019).
2. Sorrells, S. F. et al. Human hippocampal neurogenesis drops sharply in children to undetectable levels in adults. *Nature* **555**, 377–381 (2018).
3. Goncalves, J. T., Schafer, S. T. & Gage, F. H. Adult neurogenesis in the hippocampus: from stem cells to behavior. *Cell* **167**, 897–914 (2016).
4. Eriksson, P. S. et al. Neurogenesis in the adult human hippocampus. *Nat. Med.* **4**, 1313–1317 (1998).
5. Knoth, R. et al. Murine features of neurogenesis in the human hippocampus across the lifespan from 0 to 100 years. *PLoS ONE* **5**, e8809 (2010).
6. Moreno-Jimenez, E. P. et al. Adult hippocampal neurogenesis is abundant in neurologically healthy subjects and drops sharply in patients with Alzheimer's disease. *Nat. Med.* **25**, 554–560 (2019).

7. Tobin, M. K. et al. Human hippocampal neurogenesis persists in aged adults and Alzheimer's disease patients. *Cell Stem Cell* **24**, 974–982 (2019).
8. Spalding, K. L. et al. Dynamics of hippocampal neurogenesis in adult humans. *Cell* **153**, 1219–1227 (2013).
9. Shin, J. et al. Single-cell RNA-seq with waterfall reveals molecular cascades underlying adult neurogenesis. *Cell Stem Cell* **17**, 360–372 (2015).
10. Suh, H. K. et al. In vivo fate analysis reveals the multipotent and self-renewal capacities of Sox2$^+$ neural stem cells in the adult hippocampus. *Cell Stem Cell* **1**, 515–528 (2007).
11. Seri, B., Garcia-Verdugo, J. M., McEwen, B. S. & Alvarez-Buylla, A. Astrocytes give rise to new neurons in the adult mammalian hippocampus. *J. Neurosci.* **21**, 7153–7160 (2001).
12. Urban, N. et al. Return to quiescence of mouse neural stem cells by degradation of a pro-activation protein. *Science* **353**, 292–295 (2016).
13. Bonaguidi, M. A. et al. In vivo clonal analysis reveals self-renewing and multipotent adult neural stem cell characteristics. *Cell* **145**, 1142–1155 (2011).
14. Encinas, J. M. et al. Division-coupled astrocytic differentiation and age-related depletion of neural stem cells in the adult hippocampus. *Cell Stem Cell* **8**, 566–579 (2011).
15. Kempermann, G. The pessimist's and optimist's views of adult neurogenesis. *Cell* **145**, 1009–1011 (2011).
16. Pilz, G. A. et al. Live imaging of neurogenesis in the adult mouse hippocampus. *Science* **359**, 658–662 (2018).
17. Katsimpardi, L. & Lledo, P. M. Regulation of neurogenesis in the adult and aging brain. *Curr. Opin. Neurobiol.* **53**, 131–138 (2018).
18. Ben Abdallah, N. M., Slomianka, L., Vyssotski, A. L. & Lipp, H. P. Early age-related changes in adult hippocampal neurogenesis in C57 mice. *Neurobiol. Aging* **31**, 151–161 (2010).
19. Kuhn, H. G., Dickinson-Anson, H. & Gage, F. H. Neurogenesis in the dentate gyrus of the adult rat: age-related decrease of neuronal progenitor proliferation. *J. Neurosci.* **16**, 2027–2033 (1996).
20. Kalamakis, G. et al. Quiescence modulates stem cell maintenance and regenerative capacity in the aging brain. *Cell* **176**, 1407–1419 (2019).
21. Ziebell, F., Dehler, S., Martin-Villalba, A. & Marciniak-Czochra, A. Revealing age-related changes of adult hippocampal neurogenesis using mathematical models. *Development* **145**, dev153544 (2018).
22. Ahn, S. & Joyner, A. L. In vivo analysis of quiescent adult neural stem cells responding to Sonic hedgehog. *Nature* **437**, 894–897 (2005).
23. Blomfield, I. M. et al. Id4 promotes the elimination of the pro-activation factor Ascl1 to maintain quiescence of adult hippocampal stem cells. *Elife* **8**, e48561 (2019).
24. Street, K. et al. Slingshot: cell lineage and pseudotime inference for single-cell transcriptomics. *BMC Genomics* **19**, 477 (2018).
25. Dumitru, I., Neitz, A., Alfonso, J. & Monyer, H. Diazepam binding inhibitor promotes stem cell expansion controlling environment-dependent neurogenesis. *Neuron* **94**, 125–137 (2017).
26. Berg, D. A. et al. A common embryonic origin of stem cells drives developmental and adult neurogenesis. *Cell* **177**, 654–668 (2019).
27. Yuzwa, S. A. et al. Developmental emergence of adult neural stem cells as revealed by single-cell transcriptional profiling. *Cell Rep.* **21**, 3970–3986 (2017).
28. La Manno, G. et al. RNA velocity of single cells. *Nature* **560**, 494–498 (2018).
29. Bergen, V. & et al. Generalizing RNA velocity to transient cell states through dynamical modeling. *Nat. Biotechnol.* https://doi.org/10.1038/s41587-020-0591-3 (2020).
30. Hochgerner, H., Zeisel, A., Lonnerberg, P. & Linnarsson, S. Conserved properties of dentate gyrus neurogenesis across postnatal development revealed by single-cell RNA sequencing. *Nat. Neurosci.* **21**, 290–299 (2018).
31. Yang, C. P., Gilley, J. A., Zhang, G. & Kernie, S. G. *ApoE* is required for maintenance of the dentate gyrus neural progenitor pool. *Development* **138**, 4351–4362 (2011).
32. Knobloch, M. et al. Metabolic control of adult neural stem cell activity by Fasn-dependent lipogenesis. *Nature* **493**, 226–230 (2013).
33. Gut, G., Herrmann, M. D. & Pelkmans, L. Multiplexed protein maps link subcellular organization to cellular states. *Science* **361**, eaar7042 (2018).
34. Zweifel, S. et al. HOPX defines heterogeneity of postnatal subventricular zone neural stem cells. *Stem Cell Rep.* **11**, 770–783 (2018).
35. Bonaguidi, M. A., Song, J., Ming, G. L. & Song, H. A unifying hypothesis on mammalian neural stem cell properties in the adult hippocampus. *Curr. Opin. Neurobiol.* **22**, 754–761 (2012).

Methods

Transgenic animals and labeling paradigm for NSCs. Animal experiments were approved by the Cantonal Commission for Animal Experimentation of the Canton of Zurich, Switzerland in accordance with national and cantonal regulations. To generate *Gli1-Cre^{ERT2};tdTomato* mice (*Gli1-Cre$^{+/-}$Ai14$^{+/-}$*), *Gli1-Cre^{ERT2}* mice (Gli1$^{tm3(cre/ERT2)Alj}$; The Jackson Laboratory, 007913) were crossed to a homozygous CAG tdTomato (Ai14; B6.Cg-Gt(ROSA)$^{26Sortm14(CAG-tdTomato)Hze}$; The Jackson Laboratory, 007914) reporter strain. *Ascl1-Cre^{ERT2}* mice (Ascl1-CreER$^{T2+/-}$Ai14$^{+/-}$, Ascl1-Cre ERT2, Ascl1$^{tm1.1(Cre/ERT2)Jejo}$; The Jackson Laboratory, 012882) were bred with the CAG tdTomato line (Ai14; B6.Cg-Gt(ROSA)$^{26Sortm14(CAG-tdTomato)Hze}$; The Jackson Laboratory, 007914) to obtain *Ascl1-Cre^{ERT2}/tdTomato* mice for imaging. Mice were group housed in ventilated cages (21–23 °C) under a 12-h dark/light cycle with ad libitum access to food and water. The genetic background of the two mouse lines used in this study was confirmed by sequencing analysis of single-nucleotide polymorphisms in the genome, using a panel of 2,050 single-nucleotide polymorphisms (Biolytix) and compared to results from C57BL/6 and 129S control animals. *Ascl1-Cre^{ERT2}/tdTomato* mice ($n=3$) exhibited an overlap of 99.1% (C57BL/6) and 43.6% (129S) with control animals. *Gli1-Cre^{ERT2}/tdTomato* mice ($n=3$) showed an overlap of 91.5% (C57BL/6) and 46.7% (129S) with controls. At the age of 6–7 weeks, mice of mixed sex underwent the implantation of the hippocampal window. Two weeks later, sparse labeling of NSCs was achieved by single intraperitoneal (i.p.) injection of Tam (60–70 mg per kg (body weight) for *Gli1-Cre^{ERT2}/tdTomato* mice and 70–80 mg per kg (body weight) for *Ascl1-Cre^{ERT2}/tdTomato* mice; Sigma). Imaging fields of view (hereafter referred to as SPOTs) containing identified R cells were selected to obtain 10–20 SPOTs for each mouse.

Chronic hippocampal window implantation. The surgical intervention for placement of the hippocampal window was carried out in mice aged 6–7 weeks as explained in previous studies[16,36]. Briefly, above the dorsal DG (−2.0 mm posterior −1.5 mm lateral from bregma), the skin is opened and the cranial bone is locally removed (circle of 3 mm Ø). A cylinder (3 mm Ø) of cortical tissue that has been punched out using biopsy punches (Miltex) until 1.5 mm in depth (level of the corpus callosum) is aspirated using a blunt 22-gauge needle connected to an air pump until white-matter tracks are visible. As soon as no bleeding occurs anymore, the hippocampal window (3 mm Ø stainless steel cannula, 1.5 mm in height, covered by a 3-mm Ø glass coverslip; Warner Instruments) is inserted and secured in place using the stereotactic arm and stably fixed to the cranial bone with ultraviolet-cured dental cement (Ivoclar Vivadent).

In vivo two-photon imaging in the hippocampus. Chronic two-photon imaging was performed from 2 weeks after hippocampal window surgery, as described previously[16,36]. In brief, after installation of an aluminum headpost on the contralateral side of the mouse head for repeated placement of mice in a frame, mice were anesthetized with isoflurane (1.5–2% in O_2), and body temperature was measured and kept at 37 °C with a heating pad. The imaging was performed on a custom-built two-photon microscope (Movable Objective Microscope; Sutter Instrument) using a long-working distance objective (water immersion, ×16 magnification and 0.8 NA; Nikon) and equipped with a ytterbium-doped laser system at 1,045 nm and 200 fs (High-Q lasers; FemtoTrain) or a fiber oscillator laser at 1,070 nm (Fidelity-2; Coherent) to excite tdTomato-labeled cells in the DG. Emission light was detected using a photomultiplier tube (Hamamatsu) after passing a red emission filter (610/75 nm; AHF). Individual fields of view (SPOTs) containing R cells were selected and could be revisited in subsequent sessions using a coordinate system with the cannula of the window as the reference (zero position: $x=0$, $y=0$ and $z=0$). Every SPOT was imaged repeatedly by acquisition of a z-stack (512×512-pixel resolution, 2× zoom and 5-µm step-size), carefully considering and checking for all cells of the clone. All SPOTs were checked daily, and no z-stack was acquired if no changes occurred. The time spent under the microscope for the mouse was minimized (<1 h per day).

Identification and coding of lineages after processing raw imaging data. For a detailed description of the criteria used for coding of cells within clonal lineages, please refer to the methods section and supplementary table with cell type characteristics in a previously published study[16]. Briefly, all time points and z-levels of a chronically imaged SPOT were compiled into a single file, and the structural information from all z-levels was considered in coding cell types, cellular behavior and lineage relationships. The ROI manager in FIJI was used to code each individual cell at every time point throughout the compiled imaging file. Every lineage was annotated with a code by an individual researcher and double-checked by a second researcher. The coding parameters were: CellID, CellType, Uncertainty CellType, Timepoint, MotherID, Uncertainty MotherCell, SisterID, Uncertainty SisterCell and CellDeath. Only if both researchers agreed on the coding of cell type characterization or lineage transitions was this coded as certain, otherwise as semi-certain or uncertain. The resulting compiled lineage trees were again double-checked for inconsistencies with the raw imaging data.

Analysis of the lineage trees. The assembling of the tree annotations and part of the data analysis were performed in R[37] using custom-made scripts[16]. The dataset consisted of 216 (136 Gli1 and 80 Ascl1) lineages. A total of 19 Ascl1 new lineages (from 2 additional mice) were added to the Ascl1 dataset shown by Pilz et al.[16]. Two lineages from the previous dataset were excluded because of uncertainty due to imaging quality. The observed lineage behavior of newly added Ascl1-targeted cells was fully consistent with the one described before[16]. In total, 17 (6 Gli1 and 11 Ascl1) animals were used. The Gli1 dataset consists of 1,525 cells and 1,390 lineage transitions. Multiple parameters (listed below) were used to describe the behavior of the clones and to perform the hierarchical clustering of the lineage trees. The values of some parameters were calculated using the R script and then double-checked and corrected manually; the values of other parameters were calculated manually after inspection of the lineage trees. For most of the analysis, all the active clones were considered. In some cases (specified in the figure legends), some clones were excluded. Ward's hierarchical clustering method using the Euclidean similarity index was used to perform the hierarchical clustering analysis[38]. Parameters used were as follows:

- Maximum cell number: the maximum cell number reached in the clone at one (any) time point.
- Final cell number: the number of cells in the clone at the last time point of the imaging (Extended Data Fig. 2a).
- Number of successive divisions: the maximum number of successive divisions in the clone (both R and NR cells were considered).
- Self-renewal duration of R cell: the time (d) from the first R division until the last R division in the clone. Only certain R cells were considered. If the R cell disappeared after the first division, the self-renewal time was 0 (Extended Data Fig. 2a).
- Activity duration of the clone: the time (d) from the first R division until the last division of any cell (R or NR) in the clone. If the clone only divided once, the activity duration was 0.
- Number of R successive divisions: the maximum number of R successive divisions in the clone. Only certain R cells were considered (Extended Data Fig. 2a).
- Maximum R clone content: the maximum number of R cells that were present at the same (any) time point in the clone. Only certain R cells were considered.
- Persistence of the R cell in the clone: the time (d) from the beginning of the imaging to the last time point in which last R cell is seen in the clone. Only certain R cells were considered.
- Time between R divisions: the average time (d) between R divisions in the clone (excluding the first R root cell). All certain R cells were considered. If the R cell was depleted after the first division of the R root cell, the time between R divisions was 0 (Extended Data Fig. 2a).
- Time until division of R cells in successive divisions: the time (d) between divisions among different consecutive R divisions. The divisions were counted from the first neurogenic division (first asymmetric R division in the tree).
- Time until the first division of the R cell: the time (d) from the beginning of the imaging to the last time point in which the single R cell is seen before the first division. If the clone was observed with two cells at the first imaging session (2 d.p.i.), a value of 1 was assigned. This parameter was not used for the hierarchical clustering analysis.

To determine the time-dependent fraction of clones by R content and the average clone content (Fig. 2b,d), all lineage trees were first shifted to the time point of the first R cell division to align them to a common reference time point related to cell fate. The fraction of clones by R content was obtained by determining the number of clones with the respective R content and normalizing the result by the number of observed clones. This accounted for different lineage trees having different total observation times. Likewise, the average clone content was obtained by computing the average number of the respective cell type within the observed population at each time point. The same conventions were used to obtain the results shown in Extended Data Fig. 3e; when determining division types, uncertain lineage relations were included when they were binary, that is, when they associated one mother cell with exactly two daughter cells.

For the analysis of the modes of R and NR cell divisions (heat maps), only certain R and NR mother and daughter cells and certain transitions were considered. If a cell underwent cell death, the cell fate at the last time point before cell death was taken.

The time (d) between NR divisions only accounted for certain NR cells that underwent certain and semi-certain transitions. The tree visualization was performed using the igraph package of R[39]. The pheatmap package of R was used for heat map visualization[40]. PAST3 software was used for hierarchical clustering visualization. Quantification graphs were visualized using GraphPad Prism (version 8).

Immunohistochemical identification of imaged clones and confocal microscopy. After the in vivo imaging experiments were terminated, animals were anesthetized (Burprenophine) and then perfused with cold saline first, followed by 4% paraformaldehyde (PFA) in phosphate buffer. Brains were postfixed overnight and cryoprotected (30% sucrose) before being cut horizontally at a thickness of 60 µm on a cryotome (Leica SM2010R). After imaging, immunohistochemical stainings were performed with antibodies against Sox2 (1:500 dilution, goat; Santa Cruz), GFAP (1:500 dilution, mouse; Sigma), Hopx (1:500 dilution, mouse; Santa Cruz) and Ki67 (1:250 dilution, rabbit; Abcam). For further quantifications, Nestin

(1:250 dilution, mouse; BD), Sox2, GFAP and Iba1 (1:500 dilution, rabbit; WAKO) were stained on 60-µm horizontal sections (not previously imaged in vivo). Images were taken on confocal laser-scanning microscopes (Olympus FV1000 using FluoView FV1000 or Zeiss LSM800 using ZEN Pro software). A detailed list of antibodies is provided in Supplementary Table 4.

Distribution of R cells and clones within the DG. For the analysis of the distribution of recombined R cells and imaged clones within the DG, mice received a single i.p. Tam injection (60–70 mg per kg (body weight) for *Gli1-Cre^{ERT2}/tdTomato* mice and 70–80 mg per kg (body weight) for *Ascl1-Cre^{ERT2}/tdTomato* mice). Two days following the induction (2 d.p.i.) or after the in vivo imaging experiments were terminated (2 months after the induction), the mice were perfused with cold saline followed by 4% PFA in phosphate buffer. Brains were postfixed overnight and cryoprotected (30% sucrose) before being cut horizontally at a thickness of 60 µm on a cryotome (Leica SM2010R).

For the analysis of the distribution of recombined R cells 2 d.p.i., immunohistochemical stainings were performed with the antibody against Sox2 (1:500, goat; Santa Cruz) and recombined R cells were identified for being Sox2$^+$/tdTomato$^+$ and showing a radial glia morphology. The position of the recombined R cells was registered with *x* and *y* coordinates in the first five slices containing the DG (300 µm considered on *z* axis).

For the analysis of the distribution of imaged clones, the clones were recognized in slices and their position was registered taking into account the center of the clone.

Additionally, a reference point (anchor) position was registered at the bottom tip of the DG in each slice. The distance between the anchor and the top tip of the DG was calculated in each slice (max distance). Finally, the distance between the anchor and each recombined R cell or imaged clone was calculated in each slice and normalized for the maximum distance (Extended Data Fig. 1b–d).

Furthermore, using the same registered *x* and *y* coordinates the distance between each recombined R cell and all the other recombined R cells in each slice was measured (Extended Data Fig. 1e,f) at 2 d.p.i.

Multiplexed immunostaining. For analysis of protein expression of the Gli1 and Ascl1-labeled NSCs, mice received Tam injections (180 mg per kg body weight) on three consecutive days to achieve high rates of recombination. Five days following the first induction, the mice were perfused with cold saline followed by 4% PFA in phosphate buffer. The brains were postfixed in PFA overnight, then cryoprotected for 2 d. Coronal sections were cut at a thickness of 40 µm on a cryotome (Leica SM2010R). Before staining, sections were mounted in glass-bottomed 24-well plates (Cellvis P24-1.5H-N) coated with poly-D-lysine. Using the 4i technique, adapted for fresh frozen tissue[33], the tissue was stained for tdTomato (1:500, goat; Sicgen), Hopx (1:500, mouse; Santa Cruz), Ki67 (1:250; rat, eBioscience), Sox2 (1:250, rat; Invitrogen), DCX (1:300, goat; Santa Cruz), s100β (1:500, rabbit; Abcam), Id4 (1:250, rabbit; Biocheck), Mt3 (1:300, rabbit; Abcam), GFAP (1:750, chicken; Novus) and Prox1 (1:500, rabbit; Millipore). Images were acquired with a confocal laser-scanning microscope (Zeiss LSM 800 using ZEN Pro software). Between iterations of staining, antibodies were eluted from the tissue using a 0.5 M glycine-based buffer (pH 2.5) containing 3 M urea (Sigma-Aldrich), 3 M guanidinium chloride (Sigma-Aldrich) and 0.07 M TCEP-HCl (Sigma-Aldrich). During imaging, the tissue was stored in a phosphate buffer containing 0.7 M of the free radical scavenger *N*-acetyl-cysteine to prevent photoinduced crosslinking of the antibodies to their respective epitopes. A detailed list of antibodies is provided in Supplementary Table 4.

RNAscope. For the analysis of *Ascl1* mRNA levels using RNAscope, mice received a single i.p. Tam injection (80 mg per kg (body weight) for *Gli1-Cre^{ERT2}/tdTomato* mice and 90 mg per kg (body weight) for *Ascl1-Cre^{ERT2}/tdTomato* mice). Five days following the induction (5 d.p.i.), mice were perfused with 0.9% saline followed by 10% formalin. Brains were placed in 70% ethanol, embedded in paraffin and sectioned in a coronal plane at a thickness of 5 µm. The sections were then stained according to the manufacturer's recommended protocol with probes against Ascl1 and Ki67 (RNAscope Probe Mm-Ascl1-C2 and Mm-Mki67), with target retrieval performed for 15 min and Protease Plus treatment for 30 min. The HRP-C1 label (Ki67) was visualized with tyramide signal amplification (TSA)-based fluorophore Cy5 (1:1,500; Akoya Bioscience), whereas the HRP-C2 label (Ascl1) was detected with FITC (1:1,000, Akoya Bioscience). Slides were then processed for immunofluorescence using antibodies against GFAP (1:750, rat; Millipore) and tdTomato (1:250, goat; Sicgen) and counterstained with DAPI. Images were acquired using a ×40 objective on a Leica SP8 confocal. For the quantification of the RNAscope signal, two methods were used: (1) the number of dots in each cell were counted, and (2) the mean intensity of the cells was recorded.

Quantification, statistical analysis and reproducibility. The quantification of (1) immunohistochemical stainings, (2) distribution of R cells and clones within the DG, (3) different markers in the multiplexed immunostaining experiments and (4) RNAscope experiments, was performed blinded. The quantification of the immunohistochemical stainings and the distribution of R cells and clones in the DG was performed on a minimum of three animals, using 5–6 DG sections per brain (dorsal DG). The quantification of markers in multiplexed immunostaining and RNAscope experiments was performed on a minimum of three animals, using three representative DG sections per brain. Applied statistics were conducted on data from three or more biologically independent experimental replicates.

Statistical analysis of the data was performed using GraphPad Prism (version 8). A detailed report of statistical tests used, results, sample sizes and *P* values is available in Supplementary Table 5 and the figure legends. First, normality was tested, and when data did not follow a normal distribution according to the Shapiro–Wilk test, the non-parametric Mann–Whitney test was performed. Alternatively, a paired or an unpaired two-tailed *t*-test was used for mean comparison depending on the nature of the analysis (within or between subjects). $^*P<0.05$, $^{**}P<0.01$, $^{***}P<0.001$ and $^{****}P<0.0001$ were considered significant. No statistical methods were used to predetermine sample sizes, but our sample sizes were similar to those reported in previous publications[16].

Single-cell isolation. *Gli1-Cre^{ERT2}/tdTomato* or *Ascl1-Cre^{ERT2}/tdTomato* mice were injected with Tam (180 mg per kg (body weight); 3× 5-d time point; 2× 12-week time point). Five days or 12 weeks after the first Tam injection, the DG was subdissected in ice-cold HBSS. DG dissociation was performed using the Neural Tissue Dissociation Kit (P) (Miltenyi Biotec, 130-092-628) and Myelin removal beads II (Miltenyi Biotec, 130-096-733) according to the manufacturer's protocol. Hoechst 33342 (Life Technologies) was added for live-cell discrimination. The gating strategy started with a gate on the clearly identifiable population of whole cells that separated from the debris in FSC-A/SSC-A, doublets were then eliminated using a FSC-A/FSC-H gate followed by a SSC-A/SSC-H gate. Finally, live Hoechst$^-$ tdTomato$^+$ cells were selected for sorting (Extended Data Fig. 4a). Across all sorting experiments, we identified 2–3% of whole cells among which >97% were singlets containing between 2.5% and 5% of live Hoechst$^-$ tdTomato$^+$ cells. scRNA-seq of individual cells confirmed a purity of >99%. Individual Hoechst$^-$ tdTomato$^+$ cells were sorted into 384-well plates containing lysis buffer using a FACSAria III sorter (BD Biosciences). Flow cytometry data were analyzed using FlowJo (v10). Sorted plates were stored at −80 °C until library preparation.

Single-cell library preparation and sequencing. Library preparation was performed using a mosquito robot HV genomics (TTP Labtech) following the Smart-seq2 protocol[41]. Briefly, 384-well plates containing sorted single nuclei in lysis buffer were thawed, and reverse transcription with Superscript II (Life Technologies, 18064014) and PCR using KAPA Hifi HotStart ReadyMix (Kapa, KK2602) were performed with the following biotinylated primers (Qiagen): Oligodt (AA GCA GTG GTA TCA ACG CAG AGT ACT TTT TTT TTT TTT TTT TTT TTT TTT TTV N), TSO (AAG CAG TGG TAT CAA CGC AGA GTA CATr GrG + G) and ISPCR (AA GCA GTG GTA TCA ACG CAG AGT). Following RT–PCR, clean up with Agencourt AMPure XP beads (Beckman Coulter, B37419AA) was carried out, and sample concentrations were measured using Bioanalyzer (Agilent Technologies) and normalized at a concentration of 0.3 ng µl^{-1}. The Nextera XT DNA Library Prep Kit (Illumina, FC-131–1096) was used for subsequent sample preparation. Samples were subjected to a tagmentation reaction, indexing and PCR amplification. Libraries were then mixed in 384-sample pools and purified with Agencourt AMPure XP beads. Ready DNA libraries were quality controlled using D1000 Screen Tape Assay (Agilent Technologies). Samples were sequenced at the Functional Genomics Center Zurich on Illumina HiSeq 2500 or HiSeq4000 sequencers with single-end 125-bp reads.

Single-cell RNA-seq analysis. Single-end 126-nucleotide-long reads were adaptor removed and trimmed using cutadapt (v1.16) and sickle (v1.33) with default parameters. Reads were mapped against the mouse GRCm38.90 primary assembly 126 with the Ensembl GRCm38.90 GTF annotation using STAR (v2.6.0c)[42] in 'alignRead' mode. Gene-count matrices were quantified at the exon level ignoring multimappers using featureCounts from Subread (v1.6.2). RNA velocity loom files were generated with Velocyto (v0.17.17)[28] in 'run-smartseq2' mode using the Ensembl_GRCm38.90 GTF annotation. Cells were quality checked using Scater (v1.12.2)[43]. Only cells with 1,000–6,000 genes detected, less than 8% of mitochondrial reads and more than 50,000 reads were kept. In each dataset (that is, 384-well plate), cells with more or less than 1.5-fold the median read content per cell were excluded. A total of 1,465 cells passed quality-control filtering. A total of 410 cells were filtered out including: s100b$^+$Aqp4$^+$Aldh1l1$^+$ astrocytes (only detected in *Gli1-Cre^{ERT2}/tdTomato* cells), tmem119$^+$ microglia and gad1$^+$gad2$^+$ interneurons. Approximately 1,055 cells were retained for the final analysis. Seurat (v3.1.1) was used to normalize read counts, regress out the library size and mitochondrial reads proportion per cell, find variable features with the 'vst' method and integrate multiple plates (as used previously[44]), dimensionality reduce the data (principal-component analysis, *t*-SNE and UMAP), cluster cells and test for DEGs. Differential gene expression by cell type (for example, Ascl versus Gli contrast) was tested only for genes detected in at least 20% of the cells in either of the populations. Logistic regression fits with batch as the latent variable (null model) and cell type as the predictor were run using 'FindMarkers' in Seurat. *P* values were adjusted for multiple testing using the Benjamini–Hochberg method within each contrast; genes with a false discovery rate-adjusted *P* value below 0.05 were deemed significant. Batch-affected genes were similarly tested using logistic

regression with cell type as the latent variable and batch as the predictor (batch1: plates Ascl1_12wk_1, Ascl1_5day_1, Gli1_12wk, Gli1_5day_1 and Gli1_5day_2; batch2: plates Ascl1_12wk_2 and Ascl1_5day_2). Genes with no detectable effects between the two batches (false discovery rate-adjusted *P* value greater or equal to 0.05) were subjected to downstream RNA velocity analysis. RNA velocity was run with velocyto.R (v0.6) using default parameters. RNA velocities were plotted on top of Seurat's UMAP embedding; cells were colored according to Seurat's clustering results. Lineage inference analysis was performed using Slingshot (v1.3.2)[24]. For pseudotime, independent component analysis was computed with FastICA (v1.2.2). Data analysis was carried out in R (v3.6.1).

Prediction algorithm. DEGs used for the prediction of the Gli1 and Asc1 genotypes were obtained by taking the common genes between the DEG calculated for ndNSC and DEG calculated for dNSC using the edgeR package (nine genes in total). The data, containing ndNSC and dNSC cells, were split into a training set and a test set. The training set consisted of 50% of cells from the least populated class, and the corresponding number of cells was taken from the more populated class. The prediction consisted of an Ensemble pairwise classification consisting of three models: GLM, k-NN and RFC (implemented in Caret). For each model, the cross-validation was performed ten times with 10% of the training data for the parameter tuning. Each model was used to perform classification on the test set using the statistics package predict function. To ensure a better reproducibility of the prediction, the process of fitting and prediction was done 1,000 times (seeds) for each of the three models. For each seed, the data were randomly split by the same means as above to ensure that different cells were used in different seeds. The accuracy was computed by assigning a score of −1 to the cells that were wrongly classified in each seed, for each model, and +1 to the cells that were correctly classified. The final accuracy was taken by comparing the proportion of correctly and wrongly classified cells according to the score system described above.

Reporting Summary. Further information on research design is available in the Nature Research Reporting Summary linked to this article.

Data availability

All data are available from the authors on request. scRNA-seq data have been submitted into the Gene Expression Omnibus at GSE138941.

Code availability

Source code for next-generation sequencing data processing and scRNA-seq is available at https://github.com/imallona/stem_cells_hippocampus_jessberger_lab/.

References

36. Pilz, G. A. et al. Functional imaging of dentate granule cells in the adult mouse hippocampus. *J. Neurosci.* **36**, 7407–7414 (2016).
37. R Core Team. R: *A Language and Environment for Statistical Computing*. R Foundation for Statistical Computing. https://igraph.org/ (2017).
38. Picardo, M. A. et al. Pioneer GABA cells comprise a subpopulation of hub neurons in the developing hippocampus. *Neuron* **71**, 695–709 (2011).
39. Csardi, G. & Nepusz, T. The igraph software package for complex network research. *Int. J. Complex Syst.* **1695**, 38 (2006).
40. Kolde, R. *pheatmap: Pretty Heatmaps*. R package, version 1.0.8. https://CRAN.R-project.org/package=pheatmap (2015).
41. Jaeger, B. N. et al. Miniaturization of Smart-seq2 for single-cell and single-nucleus RNA sequencing. *STAR Protoc.* **1**, 100081 (2020).
42. Dobin, A. et al. STAR: ultrafast universal RNA-seq aligner. *Bioinformatics* **29**, 15–21 (2013).
43. McCarthy, D. J., Campbell, K. R., Lun, A. T. & Wills, Q. F. Scater: pre-processing, quality control, normalization and visualization of single-cell RNA-seq data in R. *Bioinformatics* **33**, 1179–1186 (2017).
44. Stuart, T. et al. Comprehensive integration of single-cell data. *Cell* **177**, 1888–1902 (2019).

Acknowledgements

This work was supported by the European Research Council (STEMBAR to S.J. and BRAINCOMPATH to F.H.), the Swiss National Science Foundation (BSCGI0_157859 and 310030_196869 to S.J.), the Zurich Neuroscience Center, the University of Zurich (UZH) Forschungskredit fellowship (B.N.J.) and the Wellcome Trust (098357/Z/12/Z to B.D.S.). L.H. was supported by a fellowship from the Francis Crick Institute. Work in the laboratory of F.G. is supported by the Francis Crick Institute, which receives its funding from Cancer Research UK (FC0010089), the UK Medical Research Council (FC0010089) and the Wellcome Trust (FC0010089; also, investigator award 106187/Z/14/Z to F.G.). We thank P. Bethge for experimental help and D. Chichung Lie for comments on the manuscript. We thank E. Yángüez López-Cano from the Functional Genomics Center Zurich (UZH and ETHZ) and the Cytometry Facility of UZH. J. Sarabia del Castillo, G. Gut, and L. Pelkmans contributed to 4i experiments.

Author contributions

S.B. performed imaging, analyzed data and cowrote the manuscript. B.N.J. performed scRNA-seq, analyzed data and cowrote the manuscript. G.A.P. performed imaging, analyzed data and cowrote the manuscript. J.D.C. performed 4i analyses. M.K. performed scRNA-seq. L.H. performed the RNAscope experiments. I.M. performed computational analyses of scRNA-seq data. V.I.K. performed computational analyses of scRNA-seq data. D.J.J. and B.D.S. contributed to the concept, performed data analyses and cowrote the manuscript. F.G. and F.H. revised the manuscript. S.J. developed the concept and wrote the manuscript.

Competing interests

The authors declare no competing interests.

Additional information

Extended data is available for this paper at https://doi.org/10.1038/s41593-020-00759-4.

Supplementary information is available for this paper at https://doi.org/10.1038/s41593-020-00759-4.

Correspondence and requests for materials should be addressed to S.J.

Peer review information *Nature Neuroscience* thanks Yukiko Gotoh, Hongjun Song and Juan Song for their contribution to the peer review of this work.

Reprints and permissions information is available at www.nature.com/reprints.

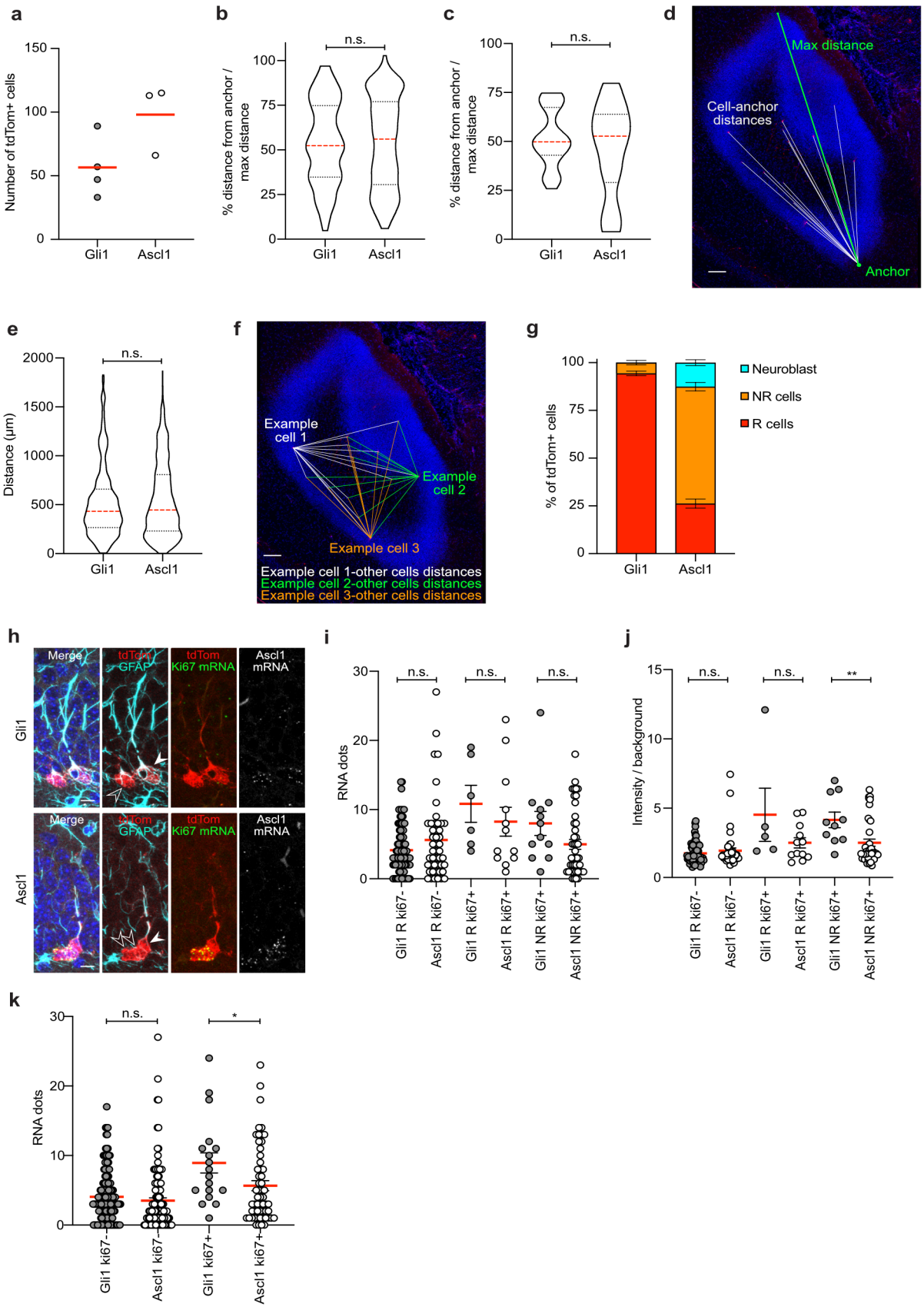

Extended Data Fig. 1 | See next page for caption.

Extended Data Fig. 1 | Characterization of Gli1 and Ascl1-targeted cells. a, Number of tdTom+ cells in the SGZ 2d after recombination in Gli1 (n = 4 mice) and Ascl1 (n = 3 mice). **b**, Percentage of the distance of tdTom+ R cells from the anchor/max distance in Gli1 and Ascl1 at 2dpi. Horizontal sections, first 300 μm of DG are considered (Gli1: 53.93 ± 2.27, n = 106 cells; Ascl1: 54.35 ± 1.83, n = 199 cells; Mann Whitney test: Mann–Whitney U = 10407; p = 0.849, two-tailed). **c**, Percentage of the distance of imaged clones from the anchor/max distance in Gli1 and Ascl1 at 2mpi. Horizontal sections (Gli1: 51.6 ± 2.31, n = 40 clones; Ascl1: 45.6 ± 5.63, n = 18 clones; Mann Whitney test: Mann-Whitney U = 337; p = 0.708, two-tailed). **d**, Representation of the method used to quantify the distances between R cells and the anchor. Horizontal view of the DG. **e**, Quantification of the distance between pairs of tdTom+ R cells in Gli1 and Ascl1 at 2dpi. Horizontal sections, first 300 μm of DG are considered (Gli1: 523.5 ± 14.86, n = 608 pair of cells; Ascl1: 546.1 ± 9.25, n = 1696 pair of cells; Mann Whitney test: Mann-Whitney U = 505390; p = 0.469, two-tailed). **f**, Representation of the method used to quantify the distances between pair of R cells (only the pairings of 3R cells with all the other R cells in the section are shown as examples). Horizontal view of the DG. **g**, Quantification of tdTom+ cell types in the SGZ 2d after recombination in Gli1 (n = 4 mice) and Ascl1 (n = 3 mice). **h**, Representative pictures of RNA-Scope with Ki67 probe (green) and Ascl1 probe (grey) and immunostaining for tdTomato (red) and GFAP (cyan) of Gli1 and Ascl1-targeted cells at 5dpi. Filled arrowheads point to R cells; empty arrowheads point to NR cells. **i**, Quantification of the Ascl1 mRNA dots of: R ki67- cells (Gli1: 4.136 ± 0.366, n = 88 cells; Ascl1: 5.617 ± 0.851, n = 47 cells; Unpaired t⁻test: t = 1.855; df = 133; p = 0.065, two-tailed), R ki67+ cells (Gli1: 10.83 ± 2.676, n = 6; Ascl1: 8.250 ± 2.089, n = 12; Unpaired t⁻test: t = 0.734; df = 16; p = 0.473, two-tailed), NR ki67+ cells (Gli1: 8.000 ± 1.741, n = 12; Ascl1: 4.978 ± 0.7160, n = 45; Unpaired t-test: t = 1.834; df = 55; p = 0.0721, two-tailed). **j**, Quantification of the Ascl1 mRNA levels (fluorescence intensity of the cell/background) of: R ki67- cells (Gli1: 1.739 ± 0.083, n = 77 cells; Ascl1: 1.933 ± 0.198, n = 40 cells; Unpaired t-test: t = 1.055; df = 115; p = 0.293, two-tailed), R ki67+ cells (Gli1: 4.528 ± 1.919, n = 5; Ascl1: 2.502 ± 0.369, n = 12; Unpaired t-test: t = 1.54; df = 15; p = 0.144, two-tailed), NR ki67+ cells (Gli1: 4.157 ± 0.566, n = 10; Ascl1: 2.510 ± 0.258, n = 39; Unpaired t-test: t = 2.815; df = 47; **p = 0.007, two-tailed). **k**, Quantification of the Ascl1 mRNA dots of: ki67- cells (Gli1: 4.067 ± 0.295, n = 149 cells; Ascl1: 3.516 ± 0.405, n = 124 cells; Unpaired t-test: t = 1.121; df = 271; p = 0.263, two-tailed), ki67+ cells (Gli1: 8.944 ± 1.454, n = 18; Ascl1: 5.667 ± 0.728, n = 57; Unpaired t-test: t = 2.141; df = 73; *p = 0.035, two-tailed). Values are shown as mean ± s.e.m. Bars in violin plots represent median and quartiles. Scale bars represent 100 μm (d,f) and 10 μm (h). For detailed statistics, see Supplementary Table 5.1.

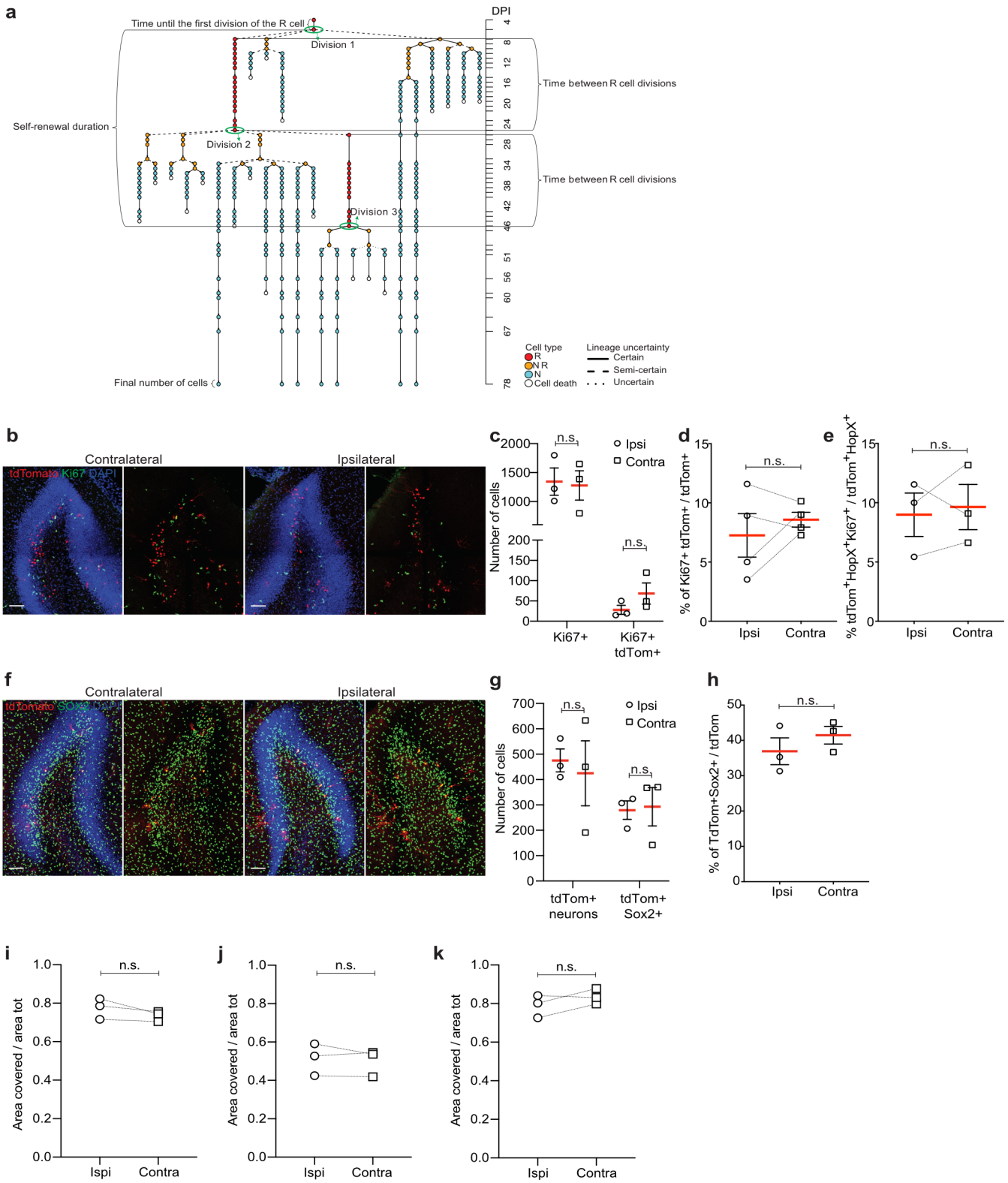

Extended Data Fig. 2 | See next page for caption.

Extended Data Fig. 2 | Intravital 2-photon imaging does not affect proliferation or lineage commitment of Gli1-targeted NSCs. a, Explanatory scheme of the different parameters extracted from lineage data of the imaged clones. **b**, Comparison of cell proliferation in contralateral and ipsilateral side in Gli1 mice after 2 months of 2-photon imaging (dorsal DG, horizontal sections). **c**, Quantification of Ki67+ cells and Ki67+ tdTom+ cells in contra- and ipsilateral side. Horizontal sections, first 360 μm of DG are considered (Ki67+ ipsilateral: 1345 ± 235.7, n = 3 mice; Ki67+ contralateral: 1278 ± 252.2, n = 3 mice; Paired t-test: t = 0.2631; df = 2; p = 0.817, two-tailed. Ki67 + /tdTom+ ipsilateral: 28 ± 11.06, n = 3 mice; Ki67 + /tdTom+ contralateral: 68.33 ± 26.1, n = 3 mice; Paired t-test: t = 2.678; df = 2; p = 0.116, two-tailed). **d**, Percentage of Ki67+ tdTom + /tdTom+ cells in contra- and ipsilateral side (ipsilateral: 7.26 ± 1.84, n = 4 mice; contralateral: 8.58 ± 0.63, n = 4 mice; Paired t-test: t = 0.895; df = 3; p = 0.436, two-tailed). **e**, Percentage of tdTom+ Hopx+ Ki67 + /tdTom+ Hopx+ cells in contra- and ipsilateral side (ipsilateral: 9.0 ± 1.83, n = 3 mice; contralateral: 9.63 ± 1.91, n = 3 mice; Paired t-test: t = 0.392; df = 2; p = 0.733, two-tailed). **f**, Comparison of the number and identity of tdTom+ cells in contralateral and ipsilateral side in Gli1 mice after 2 months of 2-photon imaging (dorsal DG, horizontal sections). **g**, Quantification of tdTom+ neurons and Sox2+ tdTom+ glial cells in contra- and ipsilateral side. Horizontal sections, first 360 μm of DG are considered (tdTom+ ipsilateral: 475.3 ± 45.16, n = 3 mice; tdTom+ contralateral: 424.7 ± 128.2, n = 3 mice; Paired t-test: t = 0.475; df = 2; p = 0.681, two-tailed. tdTom+ SOX2 + ipsilateral: 279.3 ± 36.5, n = 3 mice; tdTom+ Sox2+ contralateral: 293 ± 75.5, n = 3 mice; Paired t-test: t = 0.345; df = 2; p = 0.762, two-tailed). **h**, Percentage of Sox2+ tdTom + /tdTom+ in contra- and ipsilateral side (ipsilateral: 36.93 ± 3.78, n = 3 mice; contralateral: 41.49 ± 2.49, n = 3 mice; Paired t-test: t = 1.347; df = 2; p = 0.31, two-tailed). **i**, Quantification of the DG area covered by GFAP + cells/area tot in Gli1 contra- and ipsilateral side at 2 weeks after surgery (ipsilateral: 0.77 ± 0.03, n = 3 mice; contralateral: 0.73 ± 0.01, n = 3 mice; Paired t -test: t = 2.004; df = 2; p = 0.183, two-tailed). **j**, Quantification of the DG area covered by Iba1+ cells/area tot in Gli1 contra- and ipsilateral side at 2 weeks after surgery (ipsilateral: 0.51 ± 0.05, n = 3 mice; contralateral: 0.5 ± 0.04, n = 3 mice; Paired t-test: t = 0.677; df = 2; p = 0.568, two-tailed). **k**, Quantification of the DG area covered by GFAP + cells/area tot in Gli1 contra- and ipsilateral side at 2.5 months after surgery (ipsilateral: 0.79 ± 0.03, n = 3 mice; contralateral: 0.83 ± 0.02, n = 3 mice; Paired t-test: t = 1.654; df = 2; p = 0.24, two-tailed). Values are shown as mean ± s.e.m. Scale bars represent 100 μm (b, f). For detailed statistics, see Supplementary Table 5.1.

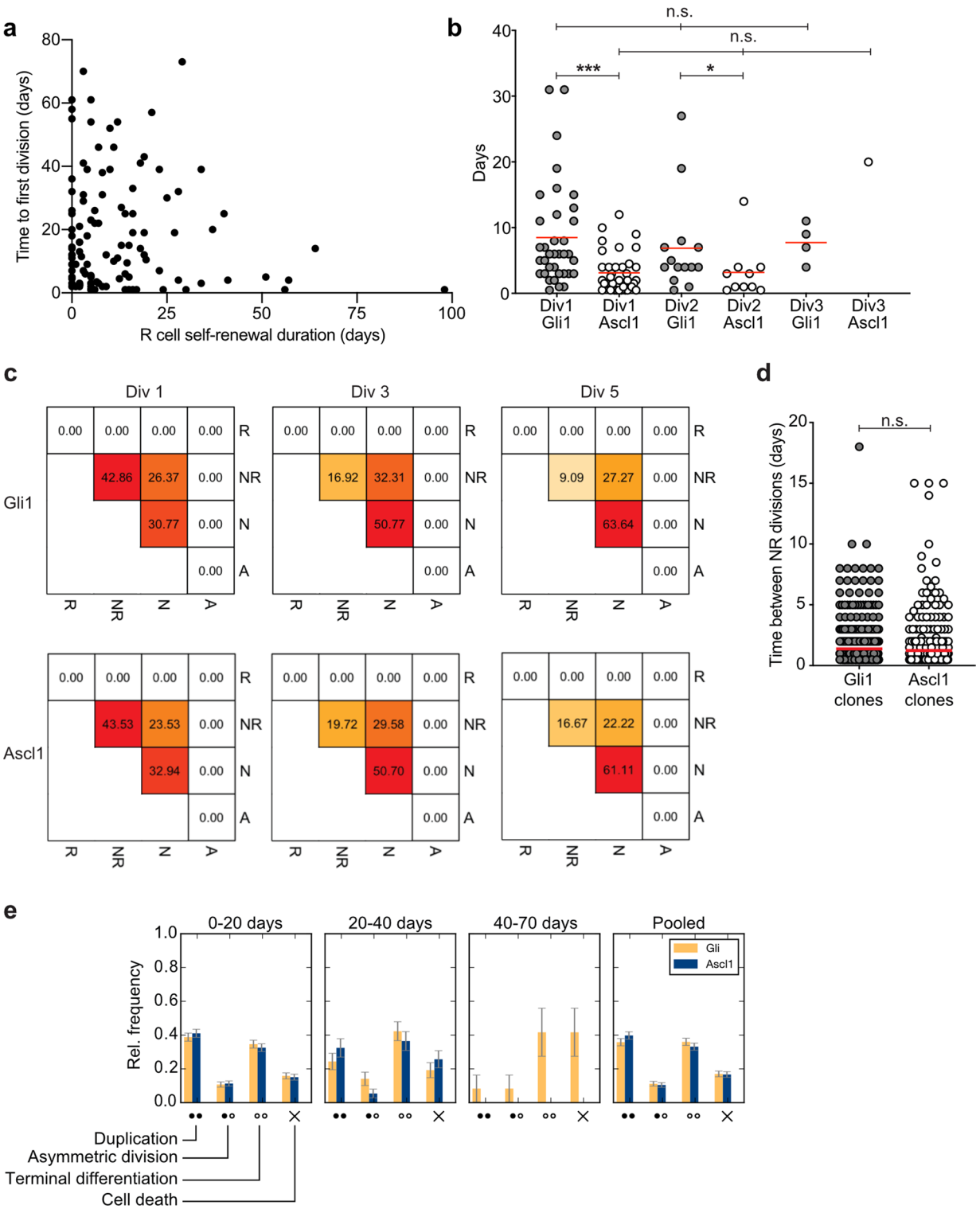

Extended Data Fig. 3 | See next page for caption.

Extended Data Fig. 3 | NR cells behavior is similar between Gli1- and Ascl1- derived lineages. a, Relationship between time to first division and R cell self-renewal duration. Gli1 and Ascl1-targeted R cells are shown as dots in the XY correlation graph (correlation analysis: Spearman $r = -0.03$, $n = 113$ XY pairs; p (two-tailed) = 0.744). **b**, Time until division of R cells (in days) in successive divisions. Div1: first division after the first neurogenic division in the clone. Comparison among consecutive divisions in each mouse line (Gli1 Div1: 8.49 ± 1.29, $n = 36$ divisions; Gli1 Div2: 6.89 ± 1.95, $n = 14$ divisions; Gli1 Div3: 7.75 ± 1.49, $n = 4$ divisions; $p = 0.511$. Ascl1 Div1: 3.12 ± 0.49, $n = 37$ divisions; Ascl1 Div2: 3.2 ± 1.28, $n = 10$ divisions; Ascl1 Div3: 20, $n = 1$ divisions; $p = 0.225$. Statistical test used: Kruskal Wallis) and comparison between Gli1 and Ascl1 (Div1: Mann Whitney test: Mann-Whitney $U = 302$; $^{***}p < 0.0001$, two-tailed; Div2: Mann Whitney test: Mann-Whitney $U = 34.5$; $^{*}p = 0.034$, two-tailed). **c**, Heat maps representing the frequencies of division modes of Gli1- and Ascl1- targeted NR cells (division rounds (Div) 1, 3 and 5 counting from the first NR division. Gli1 Div1 $n = 91$ divisions; Gli1 Div3 $n = 65$ divisions; Gli1 Div5 $n = 11$ divisions. Ascl1 Div1 $n = 85$ divisions; Ascl1 Div3 $n = 71$ divisions; Ascl1 Div5 $n = 18$ divisions). R, radial glia-like cell; NR, proliferating progenitor cell; N, neuron; A, astrocyte. Division events contain only certain lineage relations. **d**, Time (in days) between NR cell divisions (Gli1: 1.38 ± 0.08, $n = 460$ cells; Ascl1: 1.24 ± 0.08, $n = 461$ cells; Mann Whitney test: Mann-Whitney $U = 100475$; $p = 0.1207$, two-tailed). **e**, Relative frequency of the NR cells cell fate distribution. The lineage trees are shifted to the first R cell division and NR divisions are pooled according to the time windows in which they take place (Gli1 n in 0–20 days interval: 410, Gli1 n in 20–40 days interval: 78, Gli1 n in 40–70 days interval: 12; Ascl1 n in 0- 20 days interval: 424, Ascl1 n in 20–40 days interval: 74, Ascl1 n in 40–70 days interval: 0). Error bars represent the standard error of the proportion. Division events contain all binary lineage relations (certain and uncertain). Values are shown as mean ± s.e.m. For detailed statistics, see Supplementary Table 5.2.

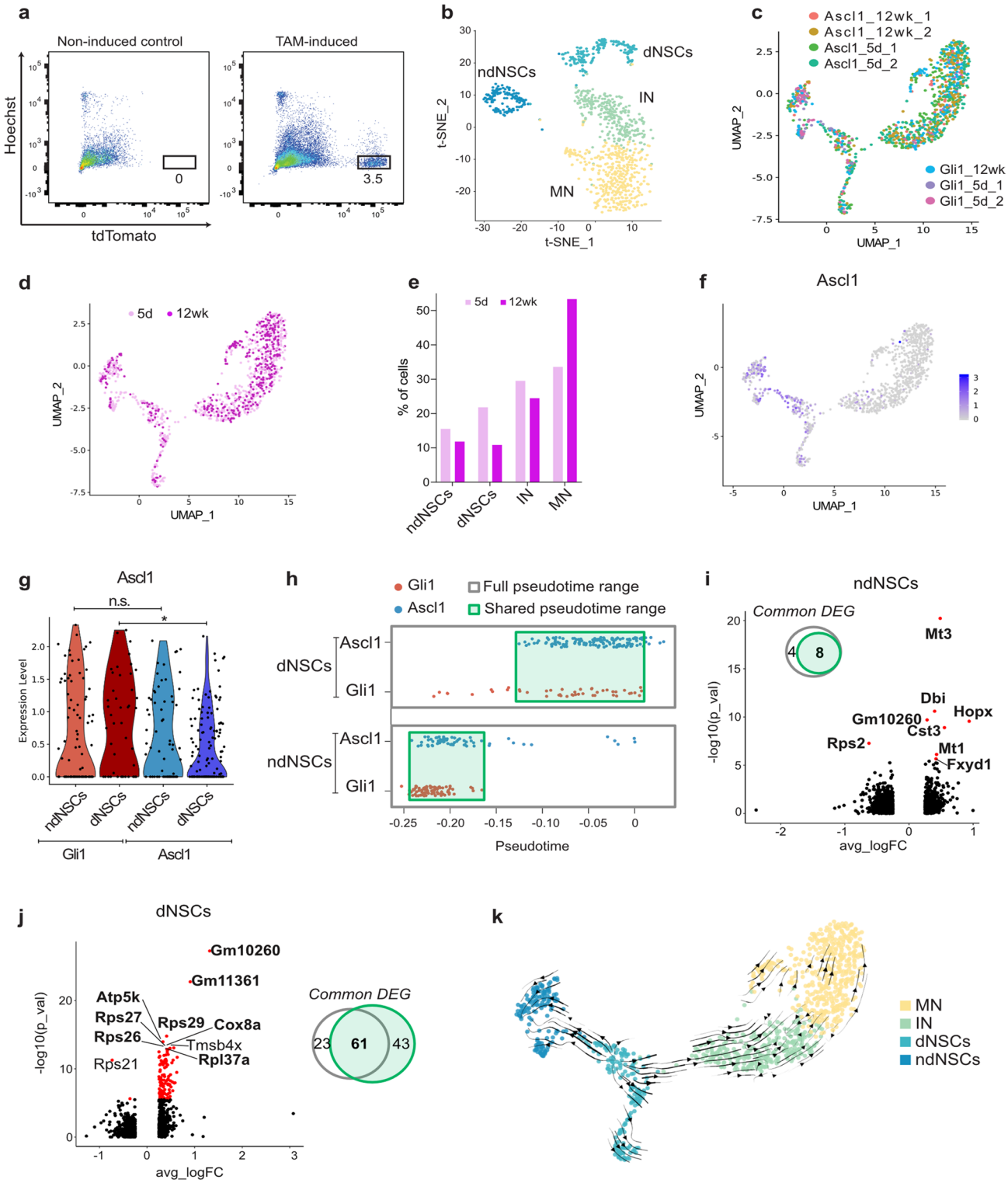

Extended Data Fig. 4 | See next page for caption.

Extended Data Fig. 4 | Transcriptional analysis of Gli1- vs Ascl1-targeted cells. a, Representative FACS plots showing gating for live (Hoechst-) tdTomato+ DG cells sorted for scRNA-seq. **b**, t-Distributed Stochastic Neighbor Embedding (t-SNE) visualization of the 4 clusters (non-dividing NSCs (ndNSCs), dividing NSCs (dNSCs), Immature Neurons (IN), Mature Neurons (MN)) identified in Gli1- and Ascl1 targeted tdTomato+ neuronal cells. **c**, Uniform Manifold Approximation and Projection (UMAP) visualization of the seven individual datasets used for analysis. _1 and _2 indicate duplicates for a given data point. **d**, UMAP visualization of the cell isolated 5 days or 12 weeks after tamoxifen injection. **e**, Distribution of the cells among the 4 clusters, 5 days or 12 weeks after tamoxifen injection. **f**, Expression pattern of Ascl1 mRNA. **g**, Violin plots showing Ascl1 mRNA levels in Gli1- and Ascl1-derived ndNSCs and dNSCs (Wilcoxon text, $^*p < 0.05$). **h**, Position of Gli1 (red) and Ascl1 (blue) ndNSCs and dNSCs along the pseudotime axis as calculated by Monocle. Cells present along the full pseudotime range (grey rectangle) or sharing the same pseudotime range (green rectangle) are depicted. **i-j**, Volcano plots showing significantly differentially expressed genes (DEGs) (red, padj < 0.05) between Gli1 or Ascl1-targeted ndNSCs (**i**) or dNSCs (**j**) when comparing only cells with shared pseudotime range. Venn diagrams indicate the overlap between DEGs found when comparing Gli1 or Ascl1-targeted ndNSCs (**i**) or dNSCs (**j**) using the full pseudotime range (grey circles) or the shared pseudotime range (green circles). Among the top 10 DEGs, bolded gene names highlight the DEGs found in both comparisons. **k**, UMAP visualization of RNA velocities calculated using scVelo. For detailed statistics, see Supplementary Table 5.3.

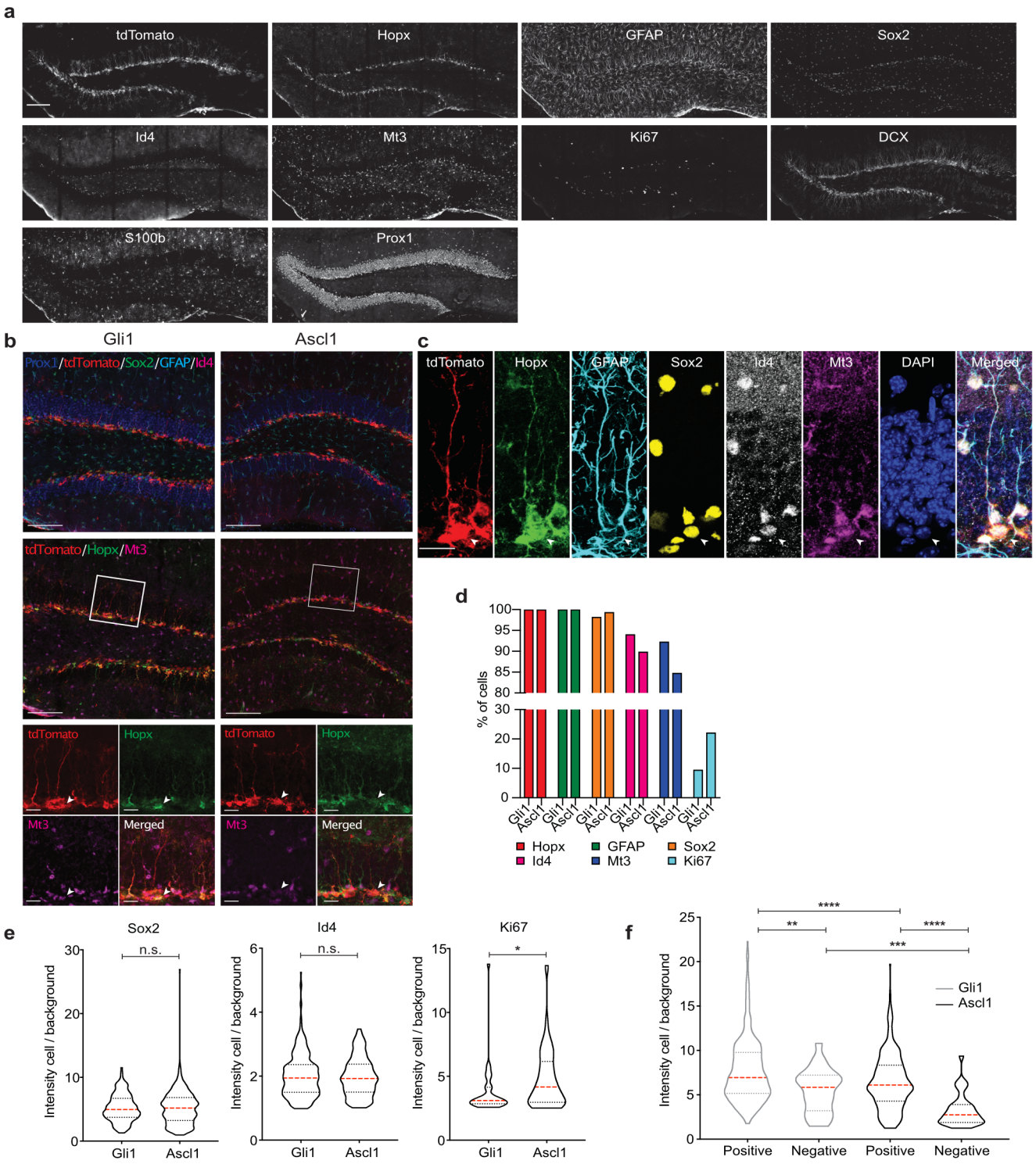

Extended Data Fig. 5 | See next page for caption.

Extended Data Fig. 5 | Stem cell markers associated with quiescence are differentially expressed between Gli1- and Ascl1-targeted NSCs. **a**, Representative example of a Gli1- tdTom DG section (5 days post tamoxifen injection) stained with multiple antibodies using the 4i protocol. Visualization of 9 different cellular markers in addition to tdTomato. Single channels are shown. **b**, Representative images of a Gli1 and an Ascl1 DG section stained using 4i protocol, 5 days post tamoxifen injection. Visualization of six different cellular markers plus tdTomato. (Top) Prox1/blue, tdTom/red, SOX2/green, GFAP/light blue, Id4/magenta. (Middle) tdTom/red, Hopx/green, Mt3/magenta. (Bottom) single channels at higher magnification (regions in the white squares). **c**, Example of a Gli1-targeted R cell stained using the 4i protocol (5 days post tamoxifen injection). Visualization of 5 different R cell markers in addition to tdTomato and DAPI. Displayed are single channels and a merged picture. **d**, Percentage of cells that express different NSC and proliferation markers in Gli1- and Ascl1-targeted R cells (Gli1 n = 330 cells; Ascl1 n = 316 cells). **e**, Quantification of Sox2 (Gli1 = 5.24 ± 0.11 n = 330 cells; Ascl1 = 5.22 ± 0.14, n = 316 cells; Mann Whitney test: Mann-Whitney U = 51100; p = 0.661, two-tailed), Id4 (Gli1 = 2.02 ± 0.03, n = 317 cells; Ascl1 = 1.98 ± 0.03, n = 285 cells; Mann Whitney test: Mann-Whitney U = 44567; p = 0.776, two-tailed) and Ki67 (Gli1 = 3.78 ± 0.36, n = 32 cells; Ascl1 = 4.82 ± 0.28, n = 69 cells; Mann Whitney test: Mann-Whitney U = 760; p = *0.011, two-tailed) protein levels (fluorescence intensity of the cell/background) in Gli1- and Ascl1-targeted R cells. **f**, Quantification of Hopx protein levels (fluorescence intensity of the cell/background) in Gli1- and Ascl1- targeted R cells that are either positive or negative for Mt3 (Gli1 positive: 7.77 ± 0.20, n = 313 cells; Gli1 negative: 5.47 ± 0.5, n = 24 cells; Whitney test: Mann-Whitney U = 2394; **p = 0.003, two-tailed. Ascl1 positive: 6.46 ± 0.18, n = 284 cells; Ascl1 negative: 3.28 ± 0.32, n = 32 cells; Whitney test: Mann-Whitney U = 1651; ****p < 0.0001, two-tailed. Gli1 positive vs Ascl1 positive: Mann Whitney test: Mann-Whitney U = 35578; ****p < 0.0001, two-tailed. Gli1 negative vs Ascl1 negative: Mann Whitney test: Mann-Whitney U = 182; ***p = 0.0006, two-tailed). Values are shown as mean ± s.e.m. Bars in violin plots represent median and quartiles. Scale bars represent 400 μm (a), 100 μm (b) and 20 μm (c, high magnification and b). For detailed statistics, see Supplementary Table 5.4.

nature research

Corresponding author(s): Sebastian Jessberger

Last updated by author(s): Nov 4, 2020

Reporting Summary

Nature Research wishes to improve the reproducibility of the work that we publish. This form provides structure for consistency and transparency in reporting. For further information on Nature Research policies, see Authors & Referees and the Editorial Policy Checklist.

Statistics

For all statistical analyses, confirm that the following items are present in the figure legend, table legend, main text, or Methods section.

n/a	Confirmed	
☐	☒	The exact sample size (*n*) for each experimental group/condition, given as a discrete number and unit of measurement
☐	☒	A statement on whether measurements were taken from distinct samples or whether the same sample was measured repeatedly
☐	☒	The statistical test(s) used AND whether they are one- or two-sided *Only common tests should be described solely by name; describe more complex techniques in the Methods section.*
☐	☒	A description of all covariates tested
☐	☒	A description of any assumptions or corrections, such as tests of normality and adjustment for multiple comparisons
☐	☒	A full description of the statistical parameters including central tendency (e.g. means) or other basic estimates (e.g. regression coefficient) AND variation (e.g. standard deviation) or associated estimates of uncertainty (e.g. confidence intervals)
☐	☒	For null hypothesis testing, the test statistic (e.g. *F*, *t*, *r*) with confidence intervals, effect sizes, degrees of freedom and *P* value noted *Give P values as exact values whenever suitable.*
☒	☐	For Bayesian analysis, information on the choice of priors and Markov chain Monte Carlo settings
☒	☐	For hierarchical and complex designs, identification of the appropriate level for tests and full reporting of outcomes
☒	☐	Estimates of effect sizes (e.g. Cohen's *d*, Pearson's *r*), indicating how they were calculated

Our web collection on statistics for biologists contains articles on many of the points above.

Software and code

Policy information about availability of computer code

Data collection

GraphPad Prism Version 8 GraphPad http://www.graphpad.com/
RRID:SCR_002798
Fiji/ImageJ Version May 2017 Fiji http://fiji.sc
RRID:SCR_002285
ZEN Version Pro Carl Zeiss AG http://www.zeiss.com/microscopy/en_us/products/microscope-software/zen.html#introduction
RRID:SCR_013672
Olympus Fluoview FV1000 Image Analysis Software Olympus/Photonics Media http://www.photonics.com/Product.aspx?PRID=47380
RRID:SCR_014215
XuvStitch XuvTools software http://www.xuvtools.org/
RRID:SCR_005894
FlowJo TreeStar https://www.flowjo.com/solutions/flowjo
RRID:SCR_008520
Smart-seq2 Picelli, 2014 https://www.illumina.com/science/sequencing-method-explorer/kits-and-arrays/smart-seq2.html

Data analysis

R v3.6.1. The R Project for Statistical Computing http://www.r-project.org/
RRID:SCR_001905
Cutadapt v1.16 Martin, 2010 https://cutadapt.readthedocs.org/
RRID:SCR_011841
Sickle v1.33 Joshi & Fass, 2011 https://github.com/najoshi/sickle
RRID:SCR_00680
STAR v2.6.0c Dobin, 2013 http://code.google.com/p/rna-star/
RRID:SCR_015899
Seurat R package (3.1.1) Satija, 2019 http://satijalab.org/seurat/
RRID:SCR_007322
Slingshot v1.3.2 Street, 2018 https://github.com/kstreet13/slingshot

RRID:SCR_017012
FastICA v1.2.2. Yuan & Oja 2004 http://www.cis.hut.fi/projects/ica/fastica/
RRID:SCR_013110
EdgeR Robinson, 2010 http://bioconductor.org/packages/edgeR/
RRID:SCR_012802
Caret Kuhn, 2019 https://topepo.github.io/caret/
Subread version v1.6.2 http://subread.sourceforge.net/
RRID:SCR_009803
iGraph version 1.2.4.1 https://igraph.org/
No RRID available (Reference #38 in our manuscript: Csardi, G. & Nepusz, T. The igraph software package for complex network research. InterJournal, Complex Systems (2006).
Velocyto version 0.17.17 http://velocyto.org/
RRID:SCR_018167

For manuscripts utilizing custom algorithms or software that are central to the research but not yet described in published literature, software must be made available to editors/reviewers. We strongly encourage code deposition in a community repository (e.g. GitHub). See the Nature Research guidelines for submitting code & software for further information.

Data

Policy information about availability of data

All manuscripts must include a data availability statement. This statement should provide the following information, where applicable:

- Accession codes, unique identifiers, or web links for publicly available datasets
- A list of figures that have associated raw data
- A description of any restrictions on data availability

All data are available from the authors at request. scRNA-seq data have been submitted into GEO (GSE138941).

Field-specific reporting

Please select the one below that is the best fit for your research. If you are not sure, read the appropriate sections before making your selection.

☒ Life sciences ☐ Behavioural & social sciences ☐ Ecological, evolutionary & environmental sciences

For a reference copy of the document with all sections, see nature.com/documents/nr-reporting-summary-flat.pdf

Life sciences study design

All studies must disclose on these points even when the disclosure is negative.

Sample size	Sample size were derived from previous studies (please refer to methods section).
Data exclusions	No data were excluded.
Replication	Experiments were replicated three times when applicable (for details please refer to methods sections). Replication experiments were successfull.
Randomization	Imaged mice were not randomized due to distinct genotypes. Single cell RNA-sequencing data were randomized for Random Forrest classifier (for details please refer to methods sections).
Blinding	Experimenters were blinded for analyses (for details please refer to methods sections).

Reporting for specific materials, systems and methods

We require information from authors about some types of materials, experimental systems and methods used in many studies. Here, indicate whether each material, system or method listed is relevant to your study. If you are not sure if a list item applies to your research, read the appropriate section before selecting a response.

Materials & experimental systems

n/a	Involved in the study
☐	☒ Antibodies
☒	☐ Eukaryotic cell lines
☒	☐ Palaeontology
☐	☒ Animals and other organisms
☒	☐ Human research participants
☒	☐ Clinical data

Methods

n/a	Involved in the study
☒	☐ ChIP-seq
☐	☒ Flow cytometry
☒	☐ MRI-based neuroimaging

Antibodies

Antibodies used

Rat anti Ki67 eBiosciences Cat# 14-5698-82
RRID:AB_10854564
Rabbit anti Ki67 Abcam Cat# ab16667
RRID:AB_302459
Goat anti DCX Santa Cruz Biotechnology Cat# sc8066
RRID:AB_2088494
Goat anti Sox2 Santa Cruz Biotechnology Cat# sc17320
RRID:AB_2286684
Rat anti Sox2 Invitrogen Cat# 14-9811-82
RRID:AB_11219471
Mouse anti Nestin BD Biosciences Cat# 556309
RRID:AB_396354
Rabbit anti s100β Abcam Cat# ab52642 RRID:AB_882426
Mouse anti Hopx Santa Cruz Cat# sc-398703
RRID:AB_2687966
Rabbit anti Id4 Biocheck Cat# BCH-9/82-12 Ref: Blomfield et al., 2019, eLife; PMID: 31552825
Rabbit anti Mt3 Abcam Cat# ab214214 (no Ref available; https://www.abcam.com/mt3-antibody-ab214314.pdf)
Chicken anti GFAP Novus Cat# NBP1-05198 Ref: Jung et al., 2020, Autophagy; PMID: 31234698
Goat anti tdTomato Sicgen Cat# AB8181-200 RRID:AB_2722750
Mouse anti GFAP Sigma Cat# 032M4779 Ref: Ohira et al., 2010, Molecular Brain; PMID: 20815922
Rabbit anti Prox1 Millipore Cat# AB5475
RRID:AB_177485
Rat anti GFAP Invitrogen Cat# 13-0300
RRID: AB_86543
Rabbit anti Iba1 WAKO Cat# 019-19741
RRID: AB_839504

Validation

Included above

Animals and other organisms

Policy information about studies involving animals; ARRIVE guidelines recommended for reporting animal research

Laboratory animals

Mouse: Gli1tm3(cre/ERT2)Alj The Jackson Laboratory Cat# 007913
Mouse: B6.Cg-Gt(ROSA)26Sortm14(CAG-tdTomato)Hze The Jackson Laboratory Cat# 007914
Mouse: Ascl1Cre ERT2,Ascl1tm1.1(Cre/ERT2)Jejo The Jackson Laboratory Cat# 012882
Mice were group housed in ventilated cages (21-23 Celsius) under a 12h dark/light cycle with ad libitum access to food and water.Mice of mixed sex were used. At the time of surgery all mice were between 6-7 weeks of age.

Wild animals

No field collected samples were used.

Field-collected samples

No field collected samples were used.

Ethics oversight

Animal experiments were approved by the Cantonal Commission for Animal Experimentation of the Canton of Zurich, Switzerland in accordance with national and cantonal regulations.

Note that full information on the approval of the study protocol must also be provided in the manuscript.

Flow Cytometry

Plots

Confirm that:

☒ The axis labels state the marker and fluorochrome used (e.g. CD4-FITC).

☒ The axis scales are clearly visible. Include numbers along axes only for bottom left plot of group (a 'group' is an analysis of identical markers).

☒ All plots are contour plots with outliers or pseudocolor plots.

☒ A numerical value for number of cells or percentage (with statistics) is provided.

Methodology

Sample preparation	5 days or 12 weeks after the first Tam injection, the dentate gyrus (DG) was sub-dissected in ice-cold HBSS. DG dissociation was performed using the Neural Tissue Dissociation Kit (P) (Miltenyi Biotecj cat #: 130-092-628) and Myelin removal beads II (Miltenyi Biotec cat #: 130-096-733) according to the manufacturer's protocol. Hoechst 33342 (Life Technologies) was added for live cell discrimination. Individual Hoechst- tdTom+ cells were sorted into 384 well plates containing lysis buffer using a FACSAria III sorter (BD Biosciences). Sorted plates were stored at -80°C until library preparation.
Instrument	FACSAria III sorter (BD Biosciences)
Software	FlowJo TreeStar https://www.flowjo.com/solutions/flowjo RRID:SCR_008520
Cell population abundance	Across all sorting experiments we identify 2-3 % of whole cells among which >97% were singlets containing between 2.5 and 5 % of live Hoechst- tdTom+ cells. scRNA-seq of individual cells confirmed a purity of >99%.
Gating strategy	The gating strategy starts with a gate on the clearly identifiable population of whole cells that separates from the debris in FSC/SSC, doublets were then eliminated using a FSC-A/FSC-H gate followed by a SSC-A/SSC-H gate, finally live Hoechst- tdTomato+ cells were selected for sorting.

☒ Tick this box to confirm that a figure exemplifying the gating strategy is provided in the Supplementary Information.